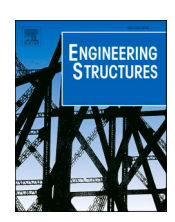
ELSEVIER

Contents lists available at ScienceDirect

Engineering Structures

journal homepage: www.elsevier.com/locate/engstruct





Integrated testing and modelling of substructures using full-field imaging and data fusion

Tobias Laux ^{a,*}, Riccardo Cappello ^a, Jack S. Callaghan ^b, Geir Ólafsson ^a, Stephen W. Boyd ^c, Duncan A. Crump ^c, Andrew F. Robinson ^c, Ole T. Thomsen ^a, Janice M. Dulieu-Barton ^{a,c}

- a Bristol Composites Institute, School of Civil, Aerospace and Design Engineering, University of Bristol, Queen's Building, University Walk, Bristol BS8 ITR, UK
- b Nuclear Futures Institute, School of Computer Science and Engineering, Bangor University, Bangor, Gwynedd LL57 2DG, UK
- ^c School of Engineering, Boldrewood Innovation Campus, University of Southampton, Southampton, UK

ARTICLE INFO

Keywords: Substructure testing Digital Image Correlation (DIC) Thermoelastic Stress Analysis (TSA) T-joint Verification and validation

ABSTRACT

A new integrated testing and modelling paradigm based on full-field imaging and finite element (FE) analysis that utilises full-field data fusion is proposed for structural evaluation and model validation at substructure level. The approach is developed for the assessment of a composite wind turbine blade (WTB) substructure subjected to multiaxial loading, mimicking in-service conditions, using a new reconfigurable loading rig. A steel mock-up equivalent to the WTB substructure was used to demonstrate the new experimental, numerical, full-field imaging, and data fusion approaches. Digital Image Correlation (DIC) and Thermoelastic Stress Analysis (TSA) were used to obtain the complex load response of the substructure. Strains and displacements derived from DIC were fused with numerical predictions obtained using a FE-based stereo-DIC simulator, which provided unparalleled like-for-like data comparisons. A numerical FEA solution for TSA was also obtained that accounts for heat transfer and allowed an independent means of structural evaluation. The challenges of deploying full-field imaging on the substructure scale are highlighted alongside procedures for mitigating multiple deleterious effects that are concatenated in large structures testing. It is demonstrated that high quality and fidelity experimental data can be obtained and fused with numerical models to provide a comprehensive and quantitative structural assessment at the substructure scale. It is shown that the proposed full-field data fusion efficiently reveals uncertainties in both the models and experiments. The work provides important steps to support virtual testing at higher length scales and their integration into the design, development, and certification programs of next generation, high-performance structures.

1. Introduction

Design, development, and certification programs for high-performance structures rely on interlinked physical testing, model predictions, and model validation across the coupon, structural detail, element, component, substructure, and full structure length scales [1]. A simplified version of the so-called 'building block' or 'testing pyramid' approach to certification is shown in Fig. 1 (a) adapted to illustrate the intent of the present paper. The traditional testing pyramid aims to de-risk the resource intensive structural design process by developing and validating the design, test, and analysis tools continuously on increasing levels of complexity and associated higher costs [2]. The approach is well established in the aerospace industry but has also been adopted by other sectors. For example, for the certification of wind

turbine blades (WTB), only coupon scale testing and a full-scale validation test are required, while utilising the intermediate tiers of the testing pyramid remains underexplored [3]. The integration/fusion of physical test data with model predictions (or virtual test data) plays a crucial role in the testing pyramid-based validation process; the ability to demonstrate a satisfactory match between model predictions and experimental results not only increases the confidence in the design and analysis tools required to ultimately demonstrate structural safety but can also provide new insights into material and structural load response and failure behaviour. It is anticipated that the need for integrated physical and virtual testing using data fusion will significantly increase at all levels of the testing pyramid with the uptake of advanced high-fidelity simulation frameworks, commonly based on the finite element (FE) method [4], [5], [6], [7], [8], [9], [10], [11] and advanced hybrid ('hardware in the loop') testing methods [12], [13], [14]. The

E-mail address: tobi.laux@bristol.ac.uk (T. Laux).

^{*} Corresponding author.

Nomenclature		y	y-coordinate
		Z	z-coordinate
DIC	Digital Image Correlation	α	coefficient of thermal expansion
FE	Finite Element	ϵ_{xx}	strain in x-direction
FEDEF	Finite Element Deformation Tool	$\epsilon_{ m yy}$	strain in y-direction
MatchID	Digital image correlation software	$arepsilon_2$	Minimum principal normal strain
MPC	Multi Point Constraint	$arepsilon_{ m v}$	von Mises equivalent strain
ROI	Region of Interest	$arepsilon_{y}$	Yield strain
RP	Reference Point	Ð	Specimen tilt angle
TSA	Thermoelastic Stress Analysis	γ_{xy}	In-plane shear strain
$c_{ m p}$	Specific heat capacity	κ	Thermal conductivity
I_1	First stress invariant	μ	mean
\boldsymbol{E}	Young's Modulus	$\mu_{ m e}$	Error map mean
f	focal length	ν	Poisson's Ratio
f_{O}	loading frequency	ho	Density
K	Thermoelastic Constant	σ	standard deviation
P_1	Load applied vertical actuator #1	σ_1	Maximum principal stress
P_3	Load applied on horizontal actuator #3	σ_2	Minimum principal stress
T_0	Mean temperature	$\sigma_{ m v}$	von Mises stress
и	displacement in x-direction	$\sigma_{ m y}$	von Mises yield strength
ν	displacement in y-direction	$\sigma_{ m e}$	Error maps standard deviation
w	displacement in z-direction	Φ	Phase
X	x-coordinate	ΔT	Thermoelastic response

overarching aim being to reduce time to market and costs associated with the introduction of new materials and design concepts essential for the development of next generation, high-performance sustainable structures. The vision behind the research is captured in Fig. 1 (a), where the intersection of the physical and virtual testing halves of the pyramid creates the requirement for new data fusion approaches to efficiently bridge the gap between the physical and virtual data domains.

The following sections of the paper describe the development of integrated testing, modelling, and data fusion approaches to structural evaluation, on the intermediate level of the testing pyramid, shown in Fig. 1 (a). The approach exploits the opportunities offered by full-field imaging techniques including Digital Image Correlation (DIC) for shape, deformation, and strain measurement [15] and infrared (IR) imaging to facilitate Thermoelastic Stress Analysis (TSA) to provide a 'stress metric' [16]. Full-field imaging and data fusion have the potential to open new avenues for integrated testing and modelling on all levels of

the testing pyramid, but the greatest benefits will accrue for testing at higher length scales, characterised by complex loads, geometry, and material configurations, and where deformation and stress fields are non-uniform and failure modes are complex. Full-field imaging techniques are ideally suited to provide the spatially rich experimental data on the substructure scale, which is difficult to obtain using traditional discrete measurement techniques such as strain gauges and linear variable differential transformers (LVDTs). However, full-field imaging of large structures is challenging and requires careful evaluation beyond what is typically required for experiments conducted on smaller samples in a universal test machine. Substructure level testing is particularly useful for composite components made from laminated, fibre-reinforced polymer (FRP) materials with stress state [17], scale [18], and manufacturing method [19] dependent properties, which result in behaviour that cannot be fully captured in coupon level tests.

While the potential of DIC, TSA, and integration with model

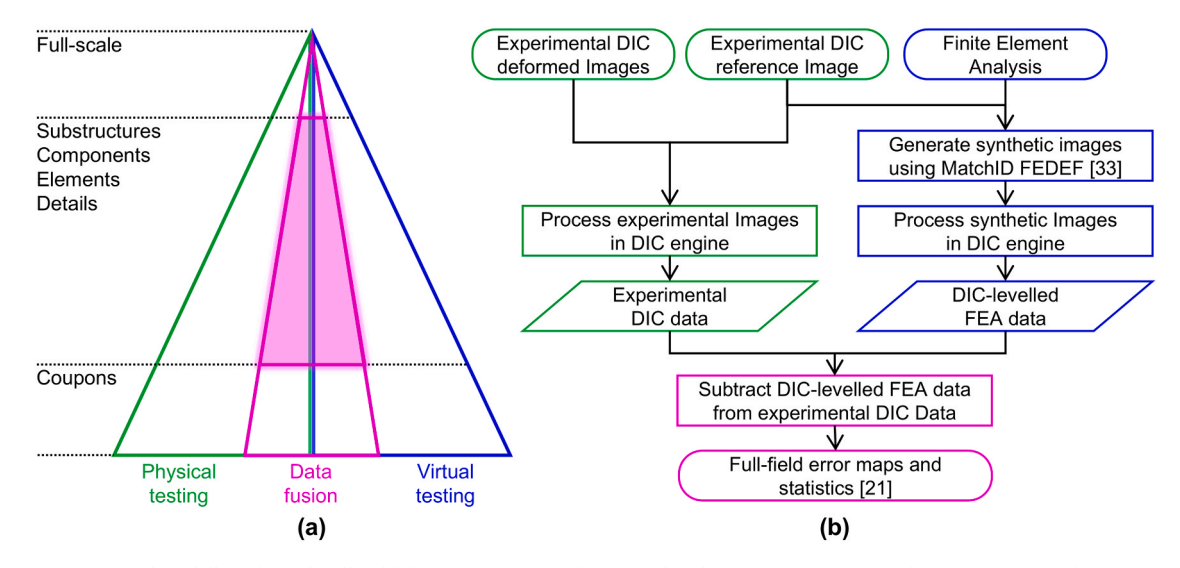


Fig. 1. Integrated testing and modelling through full-field data fusion at the substructural scale; (a) Interpretation of the future integrated testing pyramid, and (b) flowchart of full-field DIC data fusion procedure and analysis method.

predictions at higher length scales is recognised [20], [21], research is relatively sparse, as costs, timescales, and infrastructure needs associated with the design and testing of large structures can be prohibitive. Nonetheless, DIC has been used at the substructure scale to study the buckling of large composite cylindrical shells [22], the buckling of a wind turbine blade trailing edge section [23], the progressive failure of foam cored sandwich panels subjected to multiaxial loading in wind turbine blades [24], [25], the failure behaviour of large, notched, aerospace composite panels subjected to multiaxial loading [26], [27], and the failure behaviour of composite T joints [21]. DIC has also been applied to large civil structures for crack detection in bridge substructures [13], to study the seismic response of large glass façade substructures [14], and to study the effect of torsion of the progressive collapse of concrete beam columns [28]. TSA [16] is a well-established full-field experimental approach, however its application to larger scale structures has been limited largely due to the cost and robustness of the infra-red cameras. Nonetheless, there are some important exceptions where successful deployment of the techniques has taken place on wind turbine structures [29], aircraft sandwich panels [30], and for structural health monitoring [30], [31], [32].

In most of the references cited above; DIC [13], [14], [21], [22], [23], [24], [25], [26], [27], [28], and TSA; [30], [31], [32] full-field experimental data has been compared to FE model predictions. However, comprehensive, quantitative, pointwise, like-for-like comparisons are inhibited by difficulties in overcoming discrepancies between the experimental and numerical data sets with regards to coordinate system definition, spatial resolution, strain calculation algorithm, stereo system calibration error, and, crucially, the data filtering applied by the DIC procedure [33]. Systematic methods have been proposed to address inconsistencies related to coordinate system definition and spatial resolution that facilitated point-wise comparisons of DIC, TSA and FE model data, e.g. [21], [34]. However, the adopted approaches do not guarantee like-for-like comparisons as the effect of data filtering, strain calculation algorithms, stereo calibration errors, and misaligned coordinate systems are not accounted for, inducing spurious systematic discrepancies that are difficult to interpret. A new approach [33], illustrated in Fig. 1 (b), has recently been proposed that addresses all inconsistencies listed above, including those caused by the different strain calculation algorithms used in the FEA and DIC, alongside the data filtering inherent to the DIC process. Part of the approach [33], called FEDEF in the MatchID DIC software, is to process the FE data through a stereo DIC simulator that deforms the initial experimental DIC images of the specimen based on FE deformation fields, while satisfying the optical properties of the stereo imaging system. In this way, the synthetic (FE simulated) DIC images are "levelled", i.e. subjected to the same data filtering and stereo calibration errors as the experimental DIC images. Hence, like-for-like comparisons can be made between the FE and the experimental data, providing a fully quantitative comparison. Error maps and associated histograms are then generated and interpreted as proposed in [21], as illustrated by the final step in the process depicted in Fig. 1 (b). Hence, the approaches described in [21], [33] have been combined and adopted for application at the substructure scale, as described in detail in Section 4.1. and 4.3. The methodology enables a comprehensive, quantitative structural evaluation based on the interpretation of 'levelled' full-field error maps that fully exploit the spatially rich information provided by DIC and the FE modelling, while eliminating DIC process induced systematic biases. Consequentially, the outcome surpasses the level of fidelity obtained in previous studies [13], [14], [22], [23], [24], [25], [26], [27], [28]. For TSA, a similar approach as proposed in [21] is adopted for quantitative comparisons.

In summary, the overarching aim of the work described in the present paper is to realise the untapped potential of integrated testing and modelling at the components and substructure scales by advancing the current state-of-the-art in full-field imaging, data fusion, and modelling. An example of how full-field measurement errors and FE model discrepancies can be evaluated and reduced is described, showing that

comprehensive, quantitative, full-field, like-for like data comparisons can be realised on the substructure scale. To this end, full-field imaging and data fusion approaches have been developed and applied at the substructural scale in a multiaxial test that mimics the in-service loading conditions. To enable the substructural scale testing, a new facility has been created and commissioned, known as 'Structures 2025' (S2025, see acknowledgements) that consists of reconfigurable reaction frames to be fitted on a strong floor, a range of hydraulic actuators, and multiple white light and IR imaging systems, to enable high-fidelity, data rich, multiaxial testing of substructures. To demonstrate data fusion with model predictions, a virtual substructure scale experiment based on a FE model has also been constructed. Thus, insights on the way that full-field imaging and data fusion might facilitate the shift to a new paradigm in future design, development, and certification programs are provided on the intermediate and upper tiers of the testing pyramid. Although the demonstration is on a WTB substructure, the new techniques are also applicable to aerospace, automotive, marine, or construction engineering, where the fusion of full-field experimental and numerical data at a substructural scale can provide advantages over traditional approaches to structural design and validation.

2. Definition of substructure, load case, and experimental set-up

To devise the full-field imaging and data fusion approaches at the substructure scale it was necessary to select a suitable component that contained adequate challenges based on geometry, material constitution, size, and loading. Motivated by industry interest in the potentially detrimental interaction between global blade bending induced web shear loading and local cross section distortions due to the Brazier effect [35] on the failure behaviour, a WTB spar cap/web T joint was selected, as shown in Fig. 2. The flap-wise, pressure to suction side global blade bending load case (M_{PTS}) was considered for this analysis, as it is considered among the most critical WTB load cases [36]. A suitably large three-dimensional substructure (1.3 \times 1.2 \times 0.4 m) with considerable radial length (z- direction in Fig. 2) was identified and selected to capture the effect of global blade bending induced web shear deformation on the behaviour of the joint. The process to define the substructural loading representative of the global $M_{\rm PTS}$ load case is described in detail in [37], hence only a summary of the procedure is provided here. Firstly, a geometrically nonlinear shell FE model of the full blade subjected to pressure to suction side bending (M_{PTS}) was used to investigate the overall substructure deformation and the shell resultants at the interfaces between the substructure and remaining structure. The deformation of the cross section of the investigated substructure was predicted by the FE model and is shown in Fig. 3. It is observed that the cross section is laterally compressed, leading to compressive stresses in the web, and in combination with global blade torsion, to a characteristic S-shaped deformation in the web. Simple planar T-joints have been

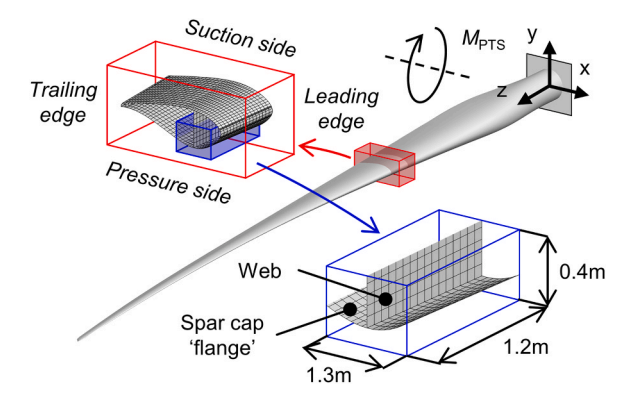


Fig. 2. Definition of wind turbine blade (WTB) spar cap/web T-joint substructure subjected to pressure to suction side bending (M_{PTS}) [37], [57].

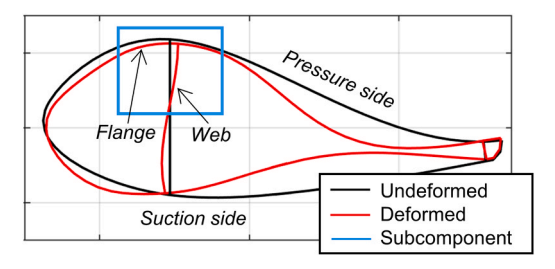


Fig. 3. Deformation of investigated cross section as predicted by the shell FE model of the full wind turbine blade subjected to a M_{PTS} bending moment (deformation not to scale) [37], [57].

investigated in several previous studies, *e.g.* in [21], [38], [39]. However, their 2D cross section and relatively simple uniaxial loading configurations are not representative of the complex deformation induced into an integrated WTB spar cap/web T-joint, as shown in Fig. 2. Hence, it was necessary to devise a new multiaxial experimental set-up to load the spar cap/web T-joint in a representative manner.

An annotated CAD model of the final experimental set-up is provided in Fig. 4. Loads were applied to the substructure via actuators #1, #2 and #3, which are denoted P_1 , P_2 and P_3 respectively. Web shear loading is applied via the horizontal actuator #3, while the vertical actuators #1 and #2 enable the application of web compression and web/flange bending. A particular and very important feature of the set-up is the pinned connection at the web edge indicated in Fig. 4 and schematically illustrated in Fig. 5. The pinned boundary condition enables the unique S-shaped deformation mode with a zero-bending moment at the inflexion point, as shown in Fig. 3. Actuators #1 and #2 in combination with the pinned connection at the web edge generate the substructural loads that mimic the complex local cross section deformation induced by the Brazier effect [35]. Other load components such as the compressive normal and in-plane shear stresses in the spar cap (flange) were disregarded to simplify the experimental set-up and the interpretation of results. This is justified, as their influence on the load response and failure behaviour of the spar cap/web T-joint is secondary to the substructural loads considered.

The pinned connection at the web edge introduces an additional

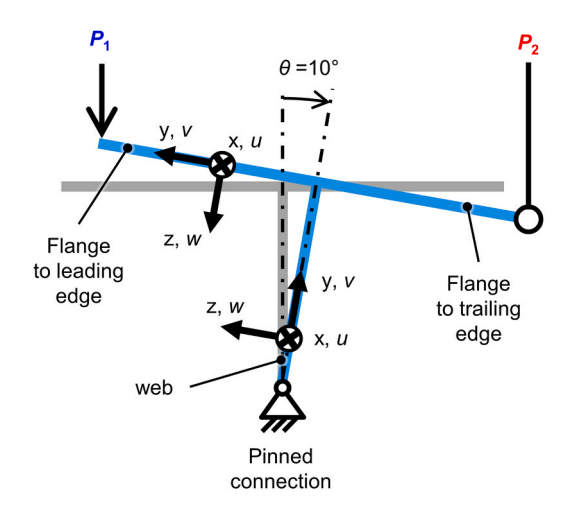


Fig. 5. Schematic of the specimen cross section with the pinned boundary condition at the web edge, definition of tilt angle θ , and web and flange coordinate systems.

testing parameter, the tilt angle θ , as shown in Fig. 5, which controls the ratio between web and flange transverse bending. Increasing θ , increases the level of transverse bending in the web relative to the flange. Using a substructural FE model similar to the one described in Section 4 of this paper, it was found that at $\theta=10^\circ$ the most representative substructure load case is achieved. The final load case is completed with actuator #2 held in a fixed position, providing another pinned connection, while P_1 and P_3 are applied in load control with a constant ratio of $P_3/P_1=0.833$.

The substructural FE model was further used to estimate failure loads based on the LaRC04 [40] and Tsai-Wu [41] failure criteria to inform actuator selection and the sizing of reaction frames. The green S2025 reaction frames shown in Fig. 4 were developed in a reconfigurable manner so that they can be used for other multiaxial large structures tests on the strong floor of the Large Structures Testing Laboratory (LSTL), part of the National Infrastructure Laboratory, at the University of Southampton. The leg-column assemblies, consisting of column, floor beam, and strut members, were sized to carry the primary reaction

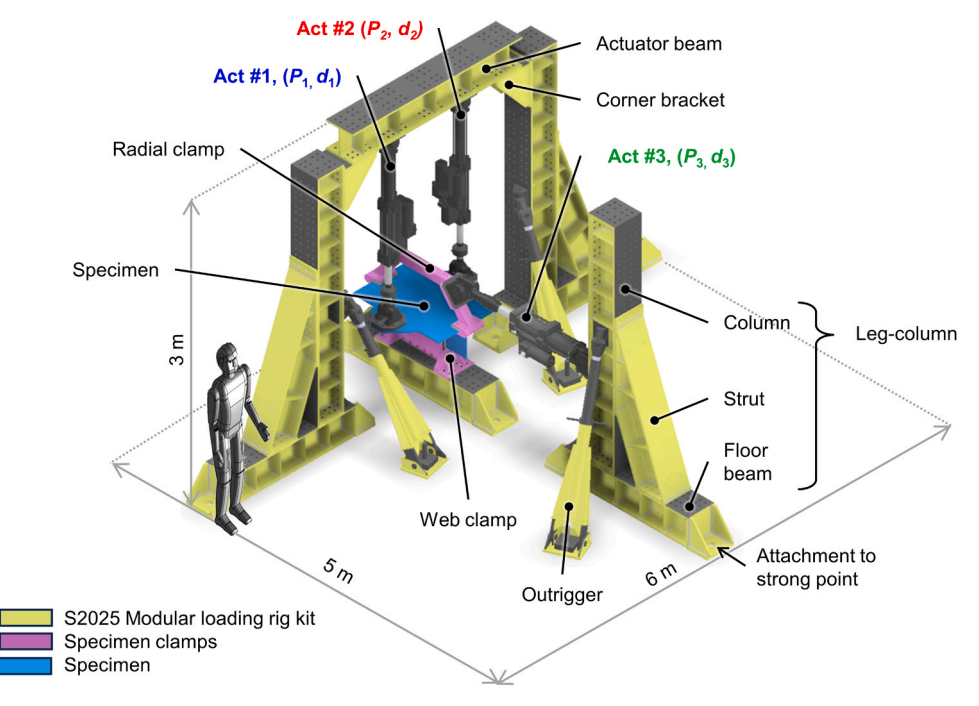


Fig. 4. Annotated CAD model of the experimental set-up.

loads. The column and strut can be attached to the floor beam in five different positions, while actuators can be attached to the column in 16 positions with a vertical spacing of 170 mm, ensuring modularity. The leg-column is designed to withstand 250 kN applied horizontally up to a maximum height of 2.5 m above the top surface of the floor beam with a factor of safety (FoS) against yielding of 1.6.1 In addition, length-adjustable outriggers are provided to absorb any lateral bending or twisting induced by out-of-plane loading. They are designed to withstand an axial load of 125 kN with a minimum FoS of 1.6 against yielding and 3 against buckling. The S2025 reconfigurable reaction frames are completed by an actuator beam and corner brackets. The reaction frames are attached to the strong floor at 1 m spaced 'strong points' using a Macalloy post-tensioning system consisting of 50 mm diameter rods pretensioned to approximately 500 kN. Individual strong points can withstand up to 500 kN in vertical tension and 250 kN in horizontal shear loading. The complete experimental set-up occupies a 5×6 m area of the strong floor and stands over 3 m tall, as shown in Fig. 4. CAD models and technical drawings of the S2025 reconfigurable reaction frames are available from the University of Bristol data repository (see data availability statement). A parametrised python script of an example leg-column and outrigger assembly for the commercially available FE software ABAQUS is also provided for preliminary sizing of new rig configurations. The only set-up specific rig parts are the specimen clamps, shown in pink in Fig. 4, which were designed to connect the specimen to the floor beam and the actuators. Details of these parts can be found in [37]. The two vertical actuators #1 and #2 are 100 kN MTS 244.22G2 actuators, and actuator #3 is a 250 kN MTS 244.31G2 actuator. All actuators are connected to a multi-station MTS FlexTest200 controller. The MTS AeroPro software was used to configure and run the test.

To commission the new multiaxial substructures test set-up, a geometrically similar steel specimen, as shown in Fig. 6(b), was devised that had similar overall dimensions, form, and matched structural stiffness components to that of the actual composite WTB structural component, as shown in Fig. 6 (a). The steel mock-up specimen provided the opportunity to conveniently develop, trial and benchmark the DIC and TSA imaging and data fusion procedures by eliminating uncertainties associated with the WTB composite material properties described in [21] that could bias the assessment of the system performance. Hence, it was used to evaluate and demonstrate the full-field imaging and data fusion approaches. A comparison between the steel and composite specimen geometry is provided in Fig. 6. Notable differences between the specimens are the web and flange thicknesses, the nature of the joint between web and flange (welded vs laminated) and the use of additional clamps required to connect actuator #1 and #2 to the composite specimen. The flange of the composite specimen consists predominantly of unidirectional layers of glass fibre reinforced polymer composites, while the web is a sandwich construction with a plywood core and GFRP face sheets made from biaxial glass/epoxy layers, as shown in Fig. 6 (c).

The steel mock-up specimen was made from two structural steel S355 plates welded at the joint, as shown in Fig. 6 (b). A detailed technical drawing is provided in Figure A.1. in the appendix. The effective bending stiffness of the laminated composite flange and web plates were obtained, accounting for the different elastic properties of the constituent materials in the composite part. The thicknesses of the web and flange steel plates were defined accordingly to provide an

equivalent bending stiffness. The approach ensures a similar compliance with regards to cross-sectional loads induced by actuator #1 (see Fig. 4), which is desirable for the assessment of the imaging systems.

Aluminium tabs were attached to the steel to interface with the web and radial friction grip clamps developed for the composite specimen, as shown in Fig. 6. The vertical actuators were bolted to the flange *via* generic adapter plates, which are part of the S2025 reconfigurable reaction frames. A detailed description of the composite specimen is provided in [37]. None of the differences have a significant influence on the test kinematics, inelastic deformation regime, and the required imaging performance, hence the steel specimen is a suitable as a surrogate for assessment of the loading and imaging procedures. The specimen, loading frames, and actuators were assembled on the LSTL strong floor using the overhead crane, a forklift, and chain hoists attached to the loading frames.

3. Loading procedure and image capture

The loading procedure and image capture sequences are schematically illustrated in Fig. 7. The stepwise loading approach was chosen to safely maximise the information obtained from a single specimen before failure, to reduce noise in the DIC images through image averaging, and to incorporate cyclic loading segments for inspection using TSA. The green boxes in Fig. 7 represent 20 DIC images taken per load step for image averaging, while the orange boxes indicate the application of cyclic loading and TSA. Three tilt angles ($\theta = 0^{\circ}, 5^{\circ}, 10^{\circ}$) were tested up to $P_1 = 25$ kN. The specimen was tilted by retracting actuator #1 in displacement control while actuators #2 and #3 were in load control, and as a consequence were continually seeking the initial, nominally zero loading condition, which resulted in a rigid body rotation. Final tilt angles were confirmed using an inclinometer positioned at the centre of the flange. To restore the specimen to its upright position, the roles of actuators #1 and #2 were reversed. Investigating three tilt angles instead of just $\theta = 10^{\circ}$, as defined in Section 2, enabled a more rigorous assessment of the experimental and FE modelling assumptions, particularly regarding the boundary conditions. Loads were applied in steps of $P_1 = 5$ kN after an initial step of $P_1 = 10$ kN. Up to $P_1 = 25$ kN, loads P_1 and $P_3 = 0.833 \times P_1$ were applied in separate increments at quasi-static loading rates of 1 kN/s to assess the induced web shear and cross section deformation individually. To take the specimen to failure, the loading procedure was modified to guarantee failure occurring under the predetermined multiaxial load case of $P_3/P_1 = 0.833$. Therefore, loads were applied concurrently at a constant ratio of $P_3/P_1 = 0.833$ at a quasistatic loading rate for P1 of 1 kN/s. To conduct TSA in between the load steps, load cycles of $P_1 = 6 \pm 5$ kN at loading frequency, f_0 , of 1 Hz were applied in load control, as indicated in orange in Fig. 7.

The region of interest (ROI) for DIC and TSA imaging was defined as the corner area between the web and the flange on the side of actuator #1, as shown in Fig. 8 (a). Local coordinate systems were defined for both the web and flange ROIs; the x and y coordinates denote the inplane directions, while the z-coordinates denote the out-of-plane directions. Fiducial markers were judicially placed, as shown in Figs. 6 and 8 (a), for spatial registration of the TSA experimental and numerical data sets and for the generation of the synthetic DIC images, as described in Section 4. The fiducials were manufactured using aluminium tape to ensure visibility in the infrared images and were placed using a selflevelling crossline laser tool. The visible light and IR cameras were arranged to image the ROIs, as shown in Fig. 8 (b); web and flange ROIs were imaged using two individual stereo DIC systems, while a single IR camera was positioned centrally to image the entire ROI. More detailed descriptions of the DIC and IR imaging systems are provided in Sections 3.1 and 3.2, respectively.

3.1. Digital image correlation (DIC)

DIC was used to obtain full-field shape (x, y, z), displacement (u, v, z)

¹ It is important to note, in other configurations where the actuators are located over 2.5 m from the floor beam, and/or at an angle, maximum safe load cases must be established on a case-by-case basis. A parametrised python script of an example leg-column and outrigger assembly for the commercially available FE software ABAQUS is provided for preliminary sizing of new rig configurations from the University of Bristol data repository (see data availability statement).

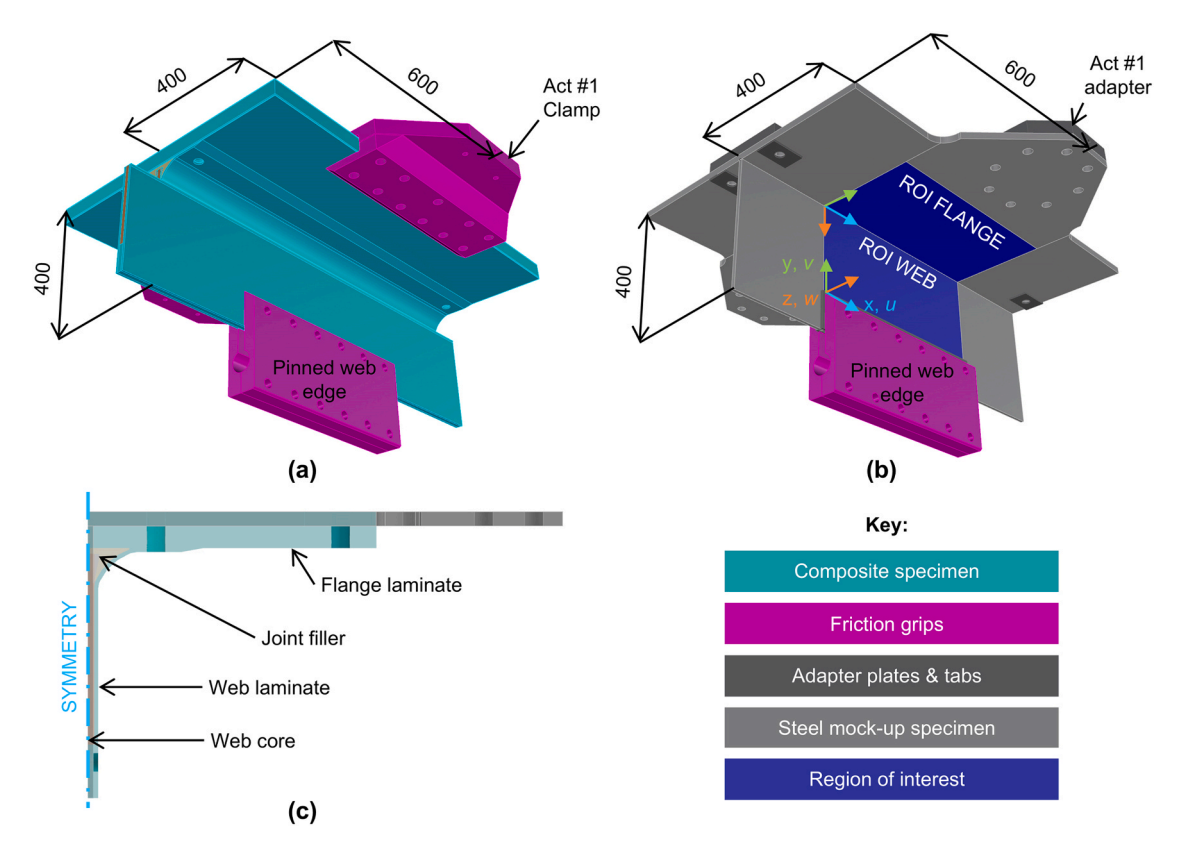


Fig. 6. Wind turbine blade substructure specimens: (a) composite T-joint, (b) steel mock up T-joint, and (c) cross-section of composite and steel specimens compared (dimensions in mm).

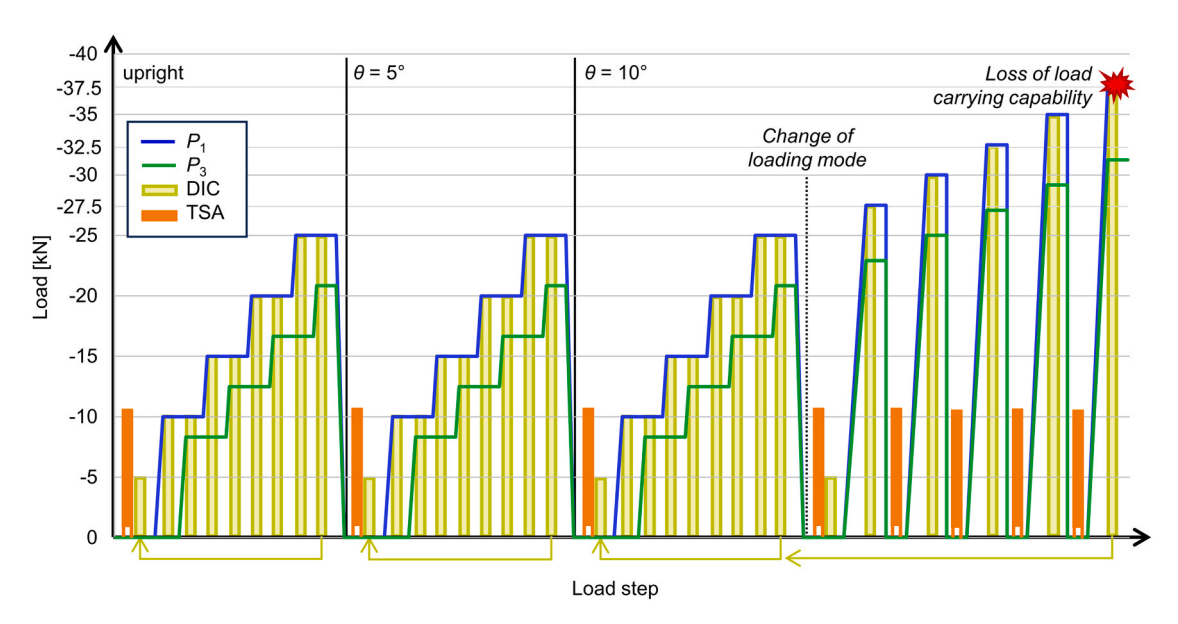


Fig. 7. Stepwise loading profile and integration with DIC/TSA imaging procedures.

w), and strain (ε_{xx} , ε_{yy} , γ_{xy}) measurements, where ε_{xx} and ε_{yy} are the inplane normal strains and γ_{xy} is the in-plane shear strain according to the coordinate systems defined in Fig. 8 (a). A commercially available DIC system from MatchID [42] was used for image acquisition and post-processing. Four Flir Blackfly BFS-U3–89S6M-C 8.9 MP cameras were employed to provide a dual stereo camera set-up to image web and flange ROIs separately. The dual camera set-up overcame the limitations of using a single stereo camera pair to image the three-dimensional T-joint. The set-up effectively removed cross-correlation and subset

tracking errors resulting from the differing perspectives and depths of field that would occur if only a single stereo pair of cameras had been used [43]. The cameras of the web stereo pair were positioned to either side of the leg-column loading frame with a stand-off distance of approximately 1 m. The flange cameras were positioned close to the floor pointing upwards, with a stand-off distance of approximately 0.5 m. In this way, the baselines of both stereo systems (distance between the cameras) were orientated approximately parallel to the imaged regions, minimising the skewness of the projection, while also

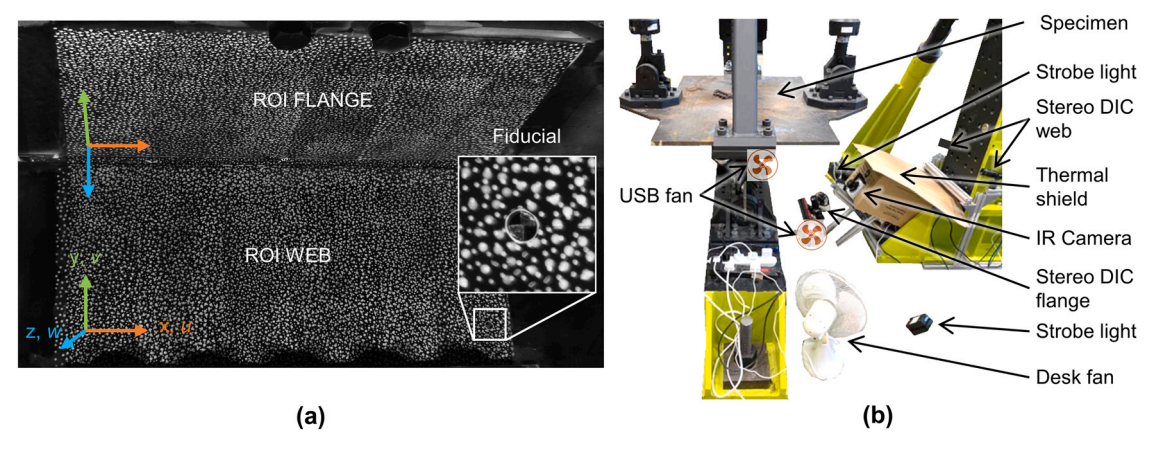


Fig. 8. Final imaging set-up: (a) ROIs and coordinate system definition, and (b) arrangement of DIC and TSA imaging systems and heat wave mitigation equipment.

relaxing the requirement for a large depth of field. The flange and web cameras were equipped with short focal length f=12 and 25 mm Computar C-mount lenses, respectively, to account for the large ROIs and limited stand-off distances, typically encountered in large structures tests. On average, this resulted in a resolution of 0.220 mm/pixel for the web ROI and 0.242 mm/pixel for the flange ROI. Illumination was provided by two GSVitec high power LED lights, positioned on the ground on both sides of the measurement space, as indicated in Fig. 8 (b), controlled by a MultiLed GX8 controller in strobing mode synchronised with the MatchID trigger box. Strobe lights were chosen to limit heat generation during imaging that drive heat convection that could have spurious effects on the DIC measurements.

The ROIs were prepared for imaging by applying a spray-painted matt black base coat. The speckle pattern, required for DIC, was then applied using white spray paint in combination with laser cut stencils. CAD files for laser cutting were computer generated using Python for Rhino [44]. The code is available from the University of Bristol data repository (see data availability statement). Two different stencils with hole sizes of 2.5 mm and 1.5 mm were overlaid, resulting in a random speckle pattern with approximately $2-3\ \text{mm}$ or $8-13\ \text{pixels}$ diameter speckles and a black/white ratio of 60 %. The choice of speckle size eliminates the risk of speckle pattern aliasing inducing systematic errors into the DIC measurement in accordance with [45]. To calibrate the stereo DIC set-up, 150 images of the MatchID calibration plate were taken covering the whole measurement space by recording images in the upright and $\theta=10^\circ$ tilted position. Initial DIC trials correlating static images of the undeformed structure revealed very high levels of noise in the displacement and strain fields, which was finally attributed to the presence of heat waves in the measurement space that distort the DIC measurements due to the temperature dependent refractive index of the turbulent hot and cold air [46]. The heat waves were identified in strain maps obtained from static images recorded at relatively high frame rate (10 Hz) as transient features of turbulence associated with hot and cold air moving across the field of view. In comparison to previous DIC experiments on the coupon scale, the effect of heat waves in the current substructural scale test was much more severe. This is attributed to the relatively poor environmental control in large structural testing halls, and the heat generated by equipment, such as cameras, lights, and hydraulic hoses, assessed to be between 40° and 60 °C, concatenating in the generation of heat waves affecting the large measurement volume between the cameras and the specimen. To mitigate some of the adverse thermal effects, following recommendations in [46], USB fans and regular desk fans, provided a constant forced convection of the air in the measurement space and a means of manipulating the flow of air. In addition, the cooling system of the IR camera generated a significant heat, which was shielded using a cardboard enclosure.

As the use of air mixing fans have been shown to affect DIC optical measurements, there is a possibility of introducing further error, rather

than reducing the error. It is therefore crucial that the effects of the air mixing fans are systematically evaluating, by determining the mean (systematic error) and standard deviation (noise) in static DIC reference images. The positive effect of the mitigation measures is illustrated in Fig. 9 by comparing the spatial mean (μ_{EXP}) and standard deviation $(\sigma_{\rm EXP})$ in the strain component measurements derived from 50 static images taken at a frame rate of 10 Hz. The mitigation measures improved strain measurements for both ROIs, but particularly for the web ROI, where noise levels were approximately halved, as shown in Fig. 9 (a). The spread of μ_{EXP} has also been reduced, indicating less potential bias in the measurements for both ROIs, as shown in Fig. 9 (b) and (d). Fig. 9 clearly demonstrates the effectiveness of the mitigation measures and highlights several important considerations regarding the accuracy and precision of DIC displacement and strain measurements, particularly in large structural tests with large measurement volumes. The stepwise loading approach shown in Fig. 7 permitted temporal image averaging and the correlation of averaged deformed and undeformed images, as suggested in [45] to further reduce aleatoric measurement noise originating from camera sensors, as well as some of the remaining deleterious effects generated by heat waves. The 20 white light images taken at 1 Hz at each loading step were averaged in Python pixel by pixel on the grey scale level. The averaged deformed images were then correlated against the static images of the corresponding tilt angles, as indicated in Fig. 7. Correlation across tilt angles, i.e. using the initial undeformed images at $\theta=0^\circ$ as the reference for all correlations, is possible but was found to induce noise and bias errors into the DIC measurement, most likely due to altered lighting conditions due to the rotation of the specimen. While this is acceptable for a qualitative assessment, it is not ideal for the quantitative assessment sought in the present study, hence images were correlated within a fixed tilt angle. All DIC post processing was carried out with a subset size of 71 px, a step size of 35 px, and a strain window of 5 subsets, resulting in a virtual strain gauge size of 211 px. A full set of post processing parameters is provided in Table A.1. in the Appendix. The subset size of 71 px guarantees a minimum of 3 to 5 speckles within a subset, ensuring uniqueness for subset matching and tracking. A standard subset size of 50 % and a strain window of 5 subsets were selected. The DIC post processing parameters were evaluated based on the standard guidelines in [45]. However, they are subcritical for this work, as strain gradients are relatively low, justifying the large subsets and strain windows used, and because the data fusion approach described in Section 4.1 for the comparison of experimental and modelling data is independent of the DIC post-processing parameters [33]. Nonetheless, the final displacement and strain noise levels are important for the interpretation of results in Sections 5 and 6. To this end, two sets of 20 static images were taken on the upright specimen that were then averaged and correlated against each other. μ_{EXP} and σ_{EXP} were evaluated for the correlated displacement and derived strain fields and are reported in Table 1. By

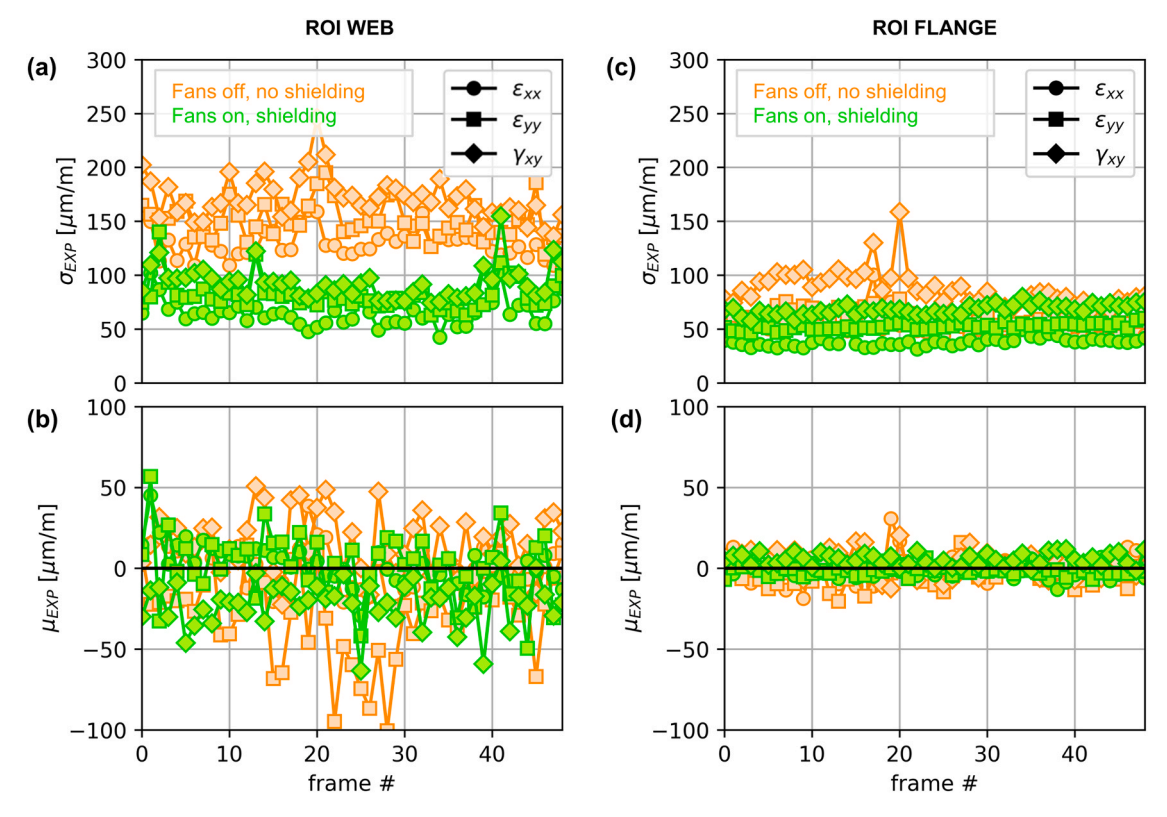


Fig. 9. Effect of heat waves on DIC strain measurement (mean and standard deviation) over 50 static images taken at $\theta = 0^{\circ}$ at 10 Hz with and without mitigation strategies in place; (a) and (b) for the web ROI and (c) and (d) for the flange ROI.

Table 1Performance of stereo DIC systems using averaged images.

		. 0
ROI	Web ($\mu_{\mathrm{EXP}} \pm \sigma_{\mathrm{EXP}}$)	Flange ($\mu_{ ext{EXP}} \pm \sigma_{ ext{EXP}}$)
и [µm]	1.57 ± 0.85	0.18 ± 0.36
ν [μm]	0.78 ± 1.26	-0.20 ± 0.58
w [μm]	2.97 ± 3.34	-0.85 ± 1.03
$\varepsilon_{\rm xx}$ [$\mu\epsilon$]	6.85 ± 21.7	-2.58 ± 10.7
ε_{vv} [$\mu\epsilon$]	-11.9 ± 24.2	-2.10 ± 16.9
γ _{xv} [με]	-2.06 ± 14.5	-0.12 ± 11.5
$ε_2$ [με]	-22.1 ± 21.5	-14.5 ± 14.9
ε _ν [με]	40.0 ± 20.3	3.4 ± 16.7

comparing the values given in Table 1 with Fig. 9 it is observed that image averaging significantly reduced the measurement noise, σ_{EXP} , in the component strains. The analysis was also carried out for the minimum principal strain (ε_2) and the von Mises equivalent strain (ε_v), as both are used qualitatively. ε_2 describes the predominantly compressive strain state on the imaged leading-edge side of the T-joint and is therefore a convenient means of visualising the strain state in a full-field plot without the need to provide all three strain components separately. $\varepsilon_{\rm v}$ is used in Section 6.3 to investigate initial yielding, as it can readily be compared to the yield strain, $\varepsilon_{\rm V}$ to assess the onset of plasticity. It is important to note that the DIC derived value of ε_v can only account for the in-plane components of the deviatoric strain tensor, as the through thickness component of strain, which could contribute to yielding, cannot be obtained from DIC. Hence, the DIC derived ε_v is a non-conservative measure to determine the onset of yielding and only provides accurate results under plane stress conditions. Furthermore, ε_2 and $\varepsilon_{\rm v}$ are derived using mathematical formulations that include square roots of differences in the strain components. Therefore, when evaluated on noisy component strain fields, non-zero strains may result, which can be spuriously interpreted as a systematic model discrepancy. The effect can be observed in Table 1, where μ_{EXP} is larger for ε_2 and ε_v than for the individual component strains. For these reasons, the quantitative full-field assessment was carried out based on component strains.

3.2. Infrared imaging and thermoelastic stress analysis (TSA)

TSA is based on the small reversible temperature change that occurs when a material is subject to transient loading, which is directly related to the first stress invariant. For a homogeneous isotropic material the reversible temperature change, ΔT , commonly referred to as the thermoelastic response [16], is related to changes in the first stress invariant, ΔI_1 , as follows:

$$\Delta T = -T_0 K \Delta I_1 \tag{1}$$

where T_o is the mean temperature of the specimen and K is the thermoelastic constant, defined as:

$$K = \frac{\alpha}{\rho C_p} \tag{2}$$

where α is the coefficient of thermal expansion, ρ is the density, and C_p is the specific heat capacity at constant pressure.

If ΔT occurs under adiabatic conditions, usually achieved by cyclic loading at relatively high frequencies of the order of 5 to 15 Hz [16], Eq. (1) provides a 'stress metric'. Therefore, TSA was used to provide an additional means (alongside the DIC) of model assessment. Changes in ΔT will primarily indicate stress is redistribution resulting from damage induced by increasing the load (see load increments Fig. 7). Permanent deformations occurring between the load steps will also cause changes in the T-joint geometry and subsequently in ΔT , and can be used to identify the onset of yielding, alongside possible changes in K [47], [48], caused by plastic deformation of the material.

The temperature field image series used for TSA was captured during the cyclic loading of the T-Joint (see Fig. 7) with a Telops FAST M2k IR camera that comprises a cooled InSb sensor (25 mK NETD). The camera frame rate was 51 Hz and images were captured over a period of 30 s. As the loading frequency was low (1 Hz), the frame rate was significantly

greater than the threshold value to satisfy the Nyquist theorem [49], [50] to enable an accurate reconstruction of the sinusoidal temperature signal in the least squares fitting algorithm. The integration time was set to 84 μs to provide a sufficient sampling period relative to the rate of change of the thermal scene without risk of image blurring. The IR camera was fitted with a 13 mm focal length lens so that the entire ROI could be imaged with a spatial resolution of approximately 2 mm/px. During thermal imaging, the fans and lights for DIC were switched off to reduce temperature perturbations. ΔT was identified from the captured thermal image series by carrying out a pixel by pixel least squares fit to the following equation:

$$T(x, y, t) = T_0 + 0.5\Delta T(x, y, t)\cos(2\pi f_0 t + \phi)$$
(3)

where T_0 is the mean temperature and f_0 is the frequency of the cycle, ϕ is the phase of ΔT with respect to the stress change, and t is time.

4. Finite element model

A FE model of the experimental set-up with the WTB steel T-joint mock-up was constructed in the commercial software Abaqus 2018 [51], as shown in Fig. 10. The FE model was used to provide physics-based predictions of deformation, stress and temperatures, which in turn were used to derive virtual experimental data for DIC and TSA (for comparison with experimental data); these processes are described in more detail in Section 4. The following provides an overview of the FE model:

(i) T-joint model and meshing

The T-joint specimen was modelled using solid elements to capture the complex local deformation in the joint region. The solid model also accounted for the welded joint, assuming perfect fillets between the web and flange plates, as shown in the insert in Fig. 10 (a). The isotropic thermomechanical material properties for structural steel S355, as provided in Table 2, were prescribed

Table 2 S355 material properties used in the FE model.

Young's Modulus, E [MPa]	210000
Poisson ratio, v [-]	0.3
Density, ρ [Kg m ⁻³]	7810
Specific heat, c_p [J Kg ⁻¹ K ⁻¹]	460
Coefficient of thermal expansion, α [K ⁻¹]	$12 imes 10^{-6}$
Thermal conductivity, κ [W m ⁻¹ K ⁻¹]	40
Yield stress, σ_y [MPa]*	355
Yield strain, ϵ_{y} [$\mu\epsilon$]*	1690

^{*} Not used in computation, for interpretation of results only.

to the discretised T-joint. The T-joint model was meshed using C3D8 brick elements with a global element size of approximately 6×6 mm and refinements in the joint region. Both web and flange plates featured a minimum of four elements through the thickness to ensure accurate prediction of bending. Reducing the global element size by half, from 12×12 mm to 6×6 mm, changed the maximum and minimum principal normal strain within the ROIs by only 1-2%, hence the model was judged to be converged. Moreover, if the model was not sufficiently refined, discrepancies between the FE model and experimental data would be apparent in the full-field error maps produced provided in Section 4.3.

(ii) Modelling strategy for complex boundary conditions

The complex experimental boundary conditions shown in Fig. 4 were replicated in the FE model by not just directly applying loads and displacement conditions to the T-joint specimen, but instead using simplified kinematic models of the actuators, swivels, and clamps to define the boundary conditions. Hence, reference point nodes (RPs) were created at the locations of pinned connections in the experiment (see Figs. 4 and 5), such as at the web clamp (RP1) and actuator swivels (RP2 – 7). The coordinates of the RPs, shown in Fig. 10, were determined from the detailed CAD model shown in Fig. 4 for the upright position of the specimen; these are reported in Table 3 so that readers can

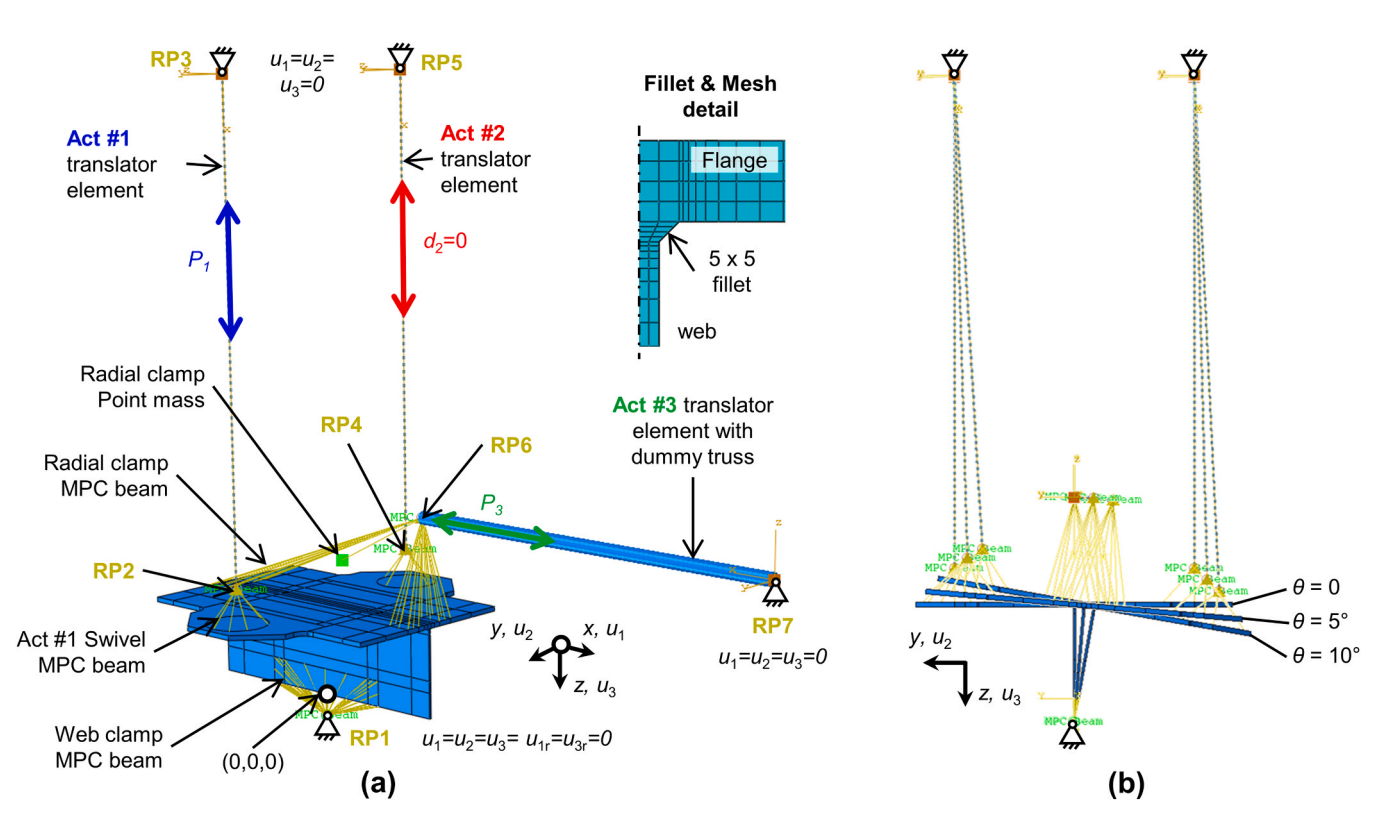


Fig. 10. Finite element modelling strategy: (a) 3D view with all model elements annotated including a fillet and mesh detail, and (b) comparison of upright and tilted models.

Table 3Coordinates of FE reference points (RPs) replicating swivels and pinned connections in the physical experimental set-up.

Reference point	Coordinates (x,y,z)	
RP1	-0,0,95	
RP2	-500, -542	
RP3	-500, -2586	
RP4	0,-500,-542	
RP5	0,-500,-2586	
RP6	568,0,-836	
RP7	2296,0,-836	

replicate the substructural FE model. The actuators were modelled using translator connector elements between RPs, which accurately mimic the actuator kinematics while providing an efficient way of applying actuator forces and displacements. The web and radial clamps were assumed to be rigid and were modelled using multi-point constraint (MPC) rigid beam links connecting the clamped (or bolted) areas of the specimen to the respective RPs. The pinned connections were replicated by coupling the translational degrees of freedom of the translator elements and the rigid beam links to their corresponding RP. Including the complex test boundary conditions (actuator kinematics and weight) was found to be necessary to reduce modelling discrepancies, uncertainty, and to achieve like-for-like comparisons to the experimental data. Their inclusion in the initial FE model enabled the investigation of more intricate differences between model and experimental data that could arise, for example, due to inaccurate material properties, inappropriate material models, insufficient mesh refinement, measurement errors, or other physical aspects.

(iii) Load steps and cases

A zero-displacement condition was applied on the translator element representing actuator #2. An initial gravity load step with a vertical acceleration of $g = 9810 \text{ mm/s}^2$ was then applied, as the horizontal actuator #3 and the radial clamp, and its tabs, have a significant mass of 422 and 118 kg, respectively. When the specimen is in a tilted condition, the mass has a measurable influence on the specimen deformation and was therefore accounted for in the FE model to ensure a like-for-like comparison to the experimental data. The mass of the radial clamp was included as a point mass positioned at its centre of gravity connected with a MPC rigid beam to the respective RP. The mass of the actuator was introduced by using a dummy truss element spanning the swivel RPs of actuator #3. The dummy truss was prescribed a density and cross-sectional area to match the overall mass of the actuator, while the stiffness was set to be negligibly small, to not affect the connector element replicating the actuator kinematics. Finally, the experimental multiaxial load cases defined in Fig. 7 were replicated by applying the corresponding actuator forces P_1 and P_3 as connector forces to the respective translator elements in a separate loading step. A geometrically nonlinear analysis scheme was selected as the application of P_1 induces significant rotation. To avoid calculation of the computationally expensive rigid rotation step itself, three separate FE models were constructed for the $\theta = 0^{\circ}$, 5° and 10° cases, as shown in Fig. 10 (b). Lastly, node sets were defined corresponding to the web and flange ROIs on the physical specimen, as defined in Figs. 6 and 8 (a), to further simplify the post processing and integration of numerical and experimental data.

4.1. FE-based virtual DIC

The full-field DIC experimental data were compared/fused data point by data point (i.e. spatial resolution defined by step size) with the

FE model predictions using the 'DIC levelling' approach proposed in [33]. The method enables quantitative, like-for-like, full-field data comparison by accounting for inconsistencies between the DIC and FE data, including different coordinate systems, data locations, strain formulation and calculation methods, spatial resolution, and data filtering. Virtual (or synthetic) deformed images were generated in a stereo-DIC simulator by deforming the real initial (or static) stereo-DIC images based on the FE mesh and the displacement fields predicted by the FE model using MatchID's Finite Element Deformation (FEDEF) tool. Prior to image deformation, the FE mesh was aligned with the DIC static images based on the fiducial markers defined in Fig. 5 for the web and flange ROIs and the three tilt angles. The virtual DIC images were then correlated using the same post-processing settings as the real/physical deformed DIC images, resulting in experimental and FE displacement and strain fields with the same data point grid, coordinate system, and DIC data filtering and smoothing artefacts. Importantly, this makes the comparison of virtual and experimental DIC independent of the choice of DIC post processing parameters and enables the efficient and fair assessment of quantities of interests in the FE model such as assumptions related to discretisation, geometry, boundary conditions, material properties, or constitutive models, to mention a few. As the reference image in the physical DIC includes deformations due to gravity, the synthetic images generated for the gravity load steps were used accordingly as the virtual DIC reference images. Despite the elaborate DIC levelling approach, 'spurious' inconsistencies between the two data sets still exist: for example, effects due to camera sensor noise, changes in the environmental conditions over time, such as ambient temperature or lighting changes, or transient heat waves. These are only captured in the physical, but not the virtual DIC data, meaning that it is expected that the DIC and FEA results will not conform exactly with each other.

4.2. FE-based virtual TSA

Two virtual TSA solutions were computed using the cyclic loading defined in Section 3. The first solution assumed adiabatic conditions, where ΔT was obtained directly using ΔI_1 in Eq. (1) predicted by the FE model. As the loading frequency was low and adiabatic conditions might not have been achieved, a second solution was considered that accounts for potential heat transfer. A coupled thermomechanical analysis was conducted by incorporating the heat generated by expansion and contraction of a material in its elastic range (i.e. the thermoelastic source) that accounts for heat diffusion by using Abaqus coupled temperature-displacement elements (C3D8T). The thermoelastic heat source was modelled using the user defined subroutine described in [52]. Three full load cycles were simulated to obtain steady state predictions of the thermoelastic response to compare with the experimental data. Each cycle was discretised in 12 time steps to capture the peak-to-peak temperature changes as a function of the applied cyclic load. The relatively fine time increments enable accurate predictions of both through thickness and in-plane heat diffusion. The thermomechanical analysis allowed quantitative comparisons of the thermoelastic response obtained from the model and experiment. Hence, there was no need to apply the relatively high cyclic loads that are usually required to generate adiabatic conditions to maintain the validity of Eq. (1), as these could not be achieved in the multiaxial test set-up due the challenge of controlling coupled actuators, inertial effects, and compliance in the load paths.

The full-field maps of the thermoelastic response obtained from the model were aligned with the experimental data using the fiducial markers that were visible in the IR images shown in Figs. 6 and 8 (a). The perspective distortion of the experimental data due to the oblique angle between the IR camera sensor and the imaged web and flange surfaces was corrected through affine transformation tools implemented in Python openCV [53] based on the known locations of the fiducial markers. As TSA relies on a thermal emission it does not suffer the same difficulties associated with perspectives as kinematic techniques such as DIC.

The thermal FE and experimental scalar field data were then interpolated on the same grid for quantitative analysis using the radial basis interpolation function implemented in Python SciPy [54].

4.3. Full-field data correlation/fusion

Full-field error maps, e, were produced by subtracting the predicted FE data fields, F^{FEM} , for each data point, i, j, from the experimental DIC or IR data fields, F^{EXP} , as:

$$\mathbf{e}(i,j) = \mathbf{F}^{\text{EXP}}(i,j) - \mathbf{F}^{\text{FEM}}(i,j) \tag{4}$$

where F denotes a DIC or IR full-field data set in form of a matrix. In DIC, F may denote a displacement field (u, v, w), a strain field $(\varepsilon_{xx}, \varepsilon_{yy}, \varepsilon_{yy}, \varepsilon_{yy})$ γ_{xy} , ε_2 , ε_v), or the fields of coordinates (x, y, z), which describe the shape of the reconstructed physical or virtual specimen. For the IR data Fdenotes $\Delta T/T_0$, as defined in Eq. (1). To further quantify the match between experimental and FE data, histograms of the error maps, e(i, j), were produced as proposed in [21] and the statistical distribution of errors was characterised by evaluating population mean, μ_e , and standard deviation, σ_e . μ_e represents the mean error in a particular variable across the ROI and is straightforward to interpret; it is expected to lie close to zero and any deviation can either be attributed to a model discrepancy and/or measurement bias. $\sigma_{\rm e}$ is a measure of the variation of the error across the field; for a perfect model, σ_e is expected to be equal to the experimental measurement noise, σ_{EXP} , as reported in Table 1. Levels of σ_e much greater than σ_{EXP} indicate either a model discrepancy and/or changes of the experimental conditions leading to increased measurement noise in comparison to the initial assessment.

5. Evaluation of initial experimental and modelling data

For an initial assessment of the experimental and modelling data, the DIC and FE ε_2 strain maps in the web and flange ROIs were compared for all load cases and tilt angles. Example strain maps are provided in Fig. 11

for $\theta=0^\circ$, 5° , 10° and the $P_1=25$ kN / $P_3=20.833$ kN load cases. It is observed from the strain maps, that the experimental and modelling data compare qualitatively well; in both data sets, increasing the tilt angle, θ , leads to increased bending in the web and decreased bending in the flange. The accurate prediction of the complex bending behaviour as a function of the tilt angle considerably raises the confidence in the selected FE modelling strategy, particularly with regards to the complex boundary conditions used in the model.

However, the error maps, e, in Fig. 11 also reveal significant differences between the experimental and modelling data. The most notable difference is the clear negative offset of the mean strain values in the web region that increases for greater tilt angles. As the offsets are clearly above the measurement noise levels in Table 1, they indicate a systematic difference between the experimental and modelling data. In the flange region, e spatially varies around a zero mean; by comparing the experimental strain patterns and error maps in Fig. 11, it is likely that the variations are driven by measurement noise, and judging from the relatively large patterns, could be artefacts from heat waves [46]. To provide a more holistic assessment of the experimental and modelling results, the error map statistics (μ_e , σ_e) are plotted as a function of the applied load cases for all three tilt angles in Fig. 12 (a) and (b), respectively. It is observed from Fig. 12 (a), that u_e stays well within \pm 50 µE for most investigated load cases. For the low load cases it is even significantly less than \pm 50 $\mu\epsilon$, indicating a good match between the experimental and modelling data, considering the measurement noise in the physical DIC in Table 1. The exception from the generally good agreement is the ε_{vv} strain component in the web; a mean absolute error that increases significantly with increasing loads to about $\mu_e \approx 200~\mu\epsilon$ unambiguously indicates a significant discrepancy between the experimental and FE model data in this area. A different trend is observed from Fig. 12 (b), where σ_e in the web is relatively low (< 60 $\mu\epsilon$) in all cases, while σ_e in the flange increases with load for all tilt angles and strain components. The trend is the strongest for $\theta = 10^{\circ}$ but it is already observed for the upright load case. The increase of σ_e with load, or the

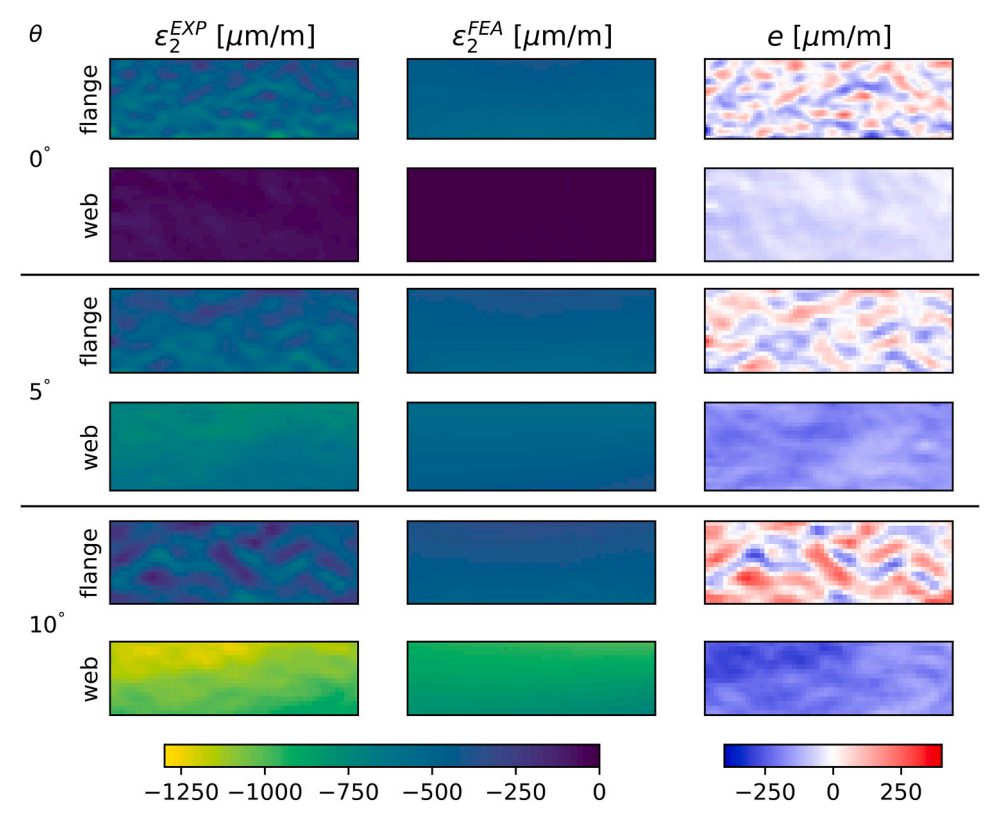


Fig. 11. Example experimental (left) and FE (centre) ε_2 strain maps with corresponding error maps, e, (right) for the $P_1=25$ kN / $P_3=20.833$ kN load case.

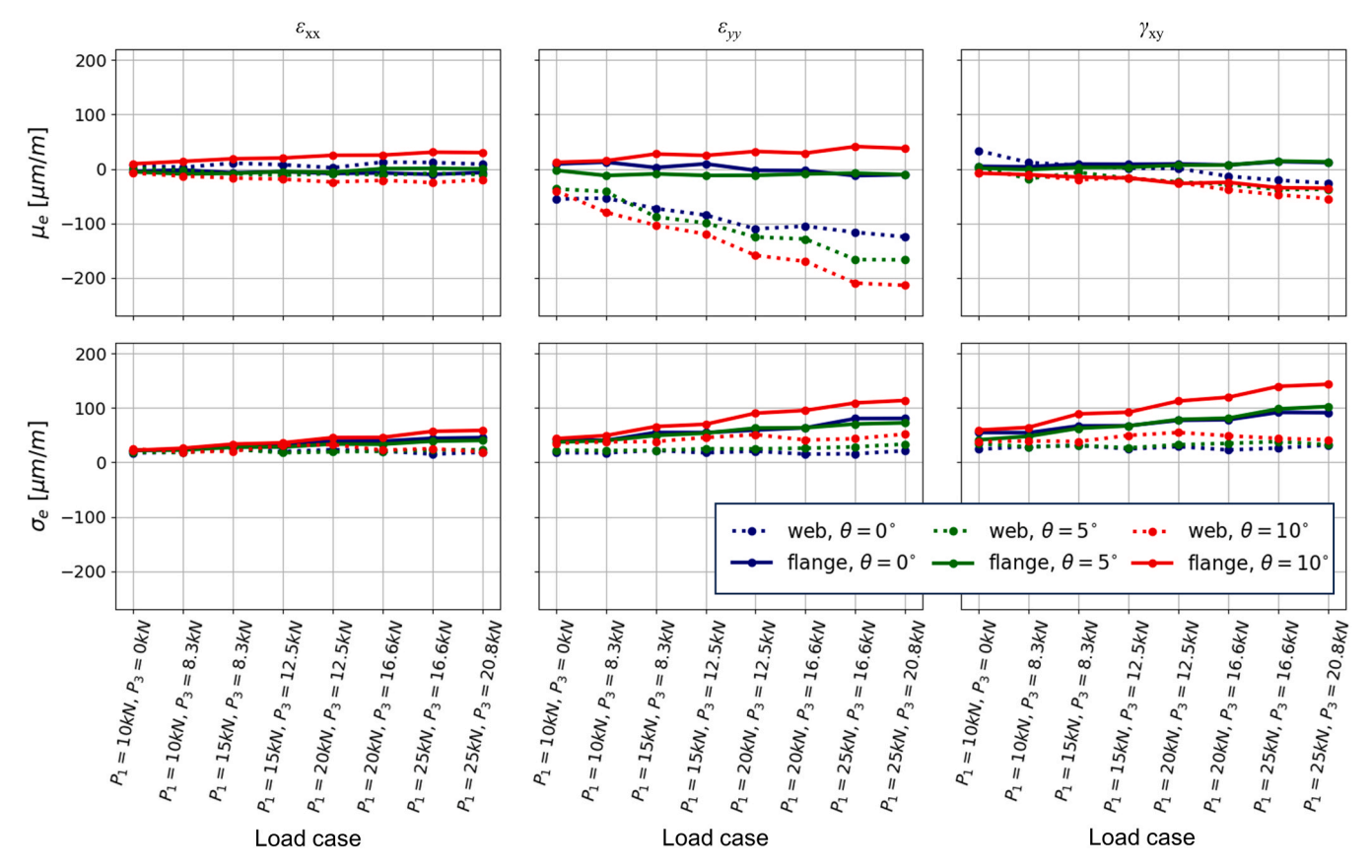


Fig. 12. Error map statistics as a function of the load case for the initial FE model; (a) mean of component strain error maps, $μ_e$, and (b) standard deviation of component strain error maps, $σ_e$.

broadening of the error map histograms, could partially be due to increased measurement uncertainty or a measurement bias, particularly because the effect is observed in all load cases and strain components. However, it could also point at another model discrepancy effecting the flange. For example, a discrepancy that leads to an approximately equal under and over prediction of the strains in different areas of the structure would lead to the observed broadening of the error map histogram. Furthermore, it is observed from Fig. 12, that errors generally increase with loading, and that the application of the vertical load P_1 induced greater errors than the horizontal load P_3 .

In summary, although the experimental and FE data qualitatively match well, the quantitative full-field assessment indicates significant discrepancies between the experimental and model data. The most notable being the clear offset between the experimental and FE ε_{yy} strains in the web ROI, hence it was decided to attempt to improve the overall match between the experimental and FE model data by focusing on addressing the ε_{vy} mismatch in the web.

After inspecting the experimental data, it was found from the reconstructed DIC z-coordinates of the unloaded specimen that the web steel plate was slightly twisted along the x-axis, as shown in Fig. 13 (a). This finding also supported the asymmetry observed in the thermoelastic response for $\theta=10^\circ$, as shown in Fig. 13 (b), indicating that the left-hand side of the web is subjected to higher stresses than the right-hand side. The twist was also confirmed by visual inspection of the specimen and implies that the initial shape of the physical T-joint specimen differs from the idealised, initial T-joint geometry assumed in the FE model. The revealed manufacturing/welding induced shape distortion was judged to be significant, and it was hypothesized that this may be the reason for the poor $\varepsilon_{\rm YY}$ match.

6. FE model update and assessment

To test the hypothesis posed in Section 5, an updated, distorted Tjoint FE model was constructed, incorporating the web twist. In addition, some flange pre-bend around the x-axis that was also observed was included. The twisted geometry was reconstructed based on the x, y, zcoordinates, i.e. the shape, of the undeformed physical specimen obtained using DIC. To this end, the coordinates in the ROI were exported form MatchID and imported in the commercial CAD software Rhinoceros 3D [44]. The twisted shape of the web was then approximated by sweeping the web cross-section along the non-parallel top and bottom edges of the reconstructed web shape. Note that the geometry outside of the ROI is extrapolated and that the new model geometry is not a perfect match, but just a better approximation of the actual T-joint shape. The improved CAD model was then inserted in the FE modelling framework shown in Fig. 10 and analysed in the exact same way as the initial T-joint model. The full-field data fusion approaches for DIC and TSA described in Section 4 were then applied to the updated (distorted) FE model to assess the initial hypothesis that the mismatch of the initial geometry was the main reason for the discrepancy between the experimental and initial FE model data.

6.1. DIC based evaluation

A first confirmation that the updated web geometry in the FE model approximated the physical specimen more closely than the initial model was obtained by comparing the z-coordinate fields and associated error maps, *e*, as shown in Fig. 14. It is straightforward to observe that the twisted web geometry is captured more accurately in the updated FE model and that model shape discrepancies are reduced in comparison to the initial FE model, as indicated by the error maps.

To assess the improvements in more detail, combined strain

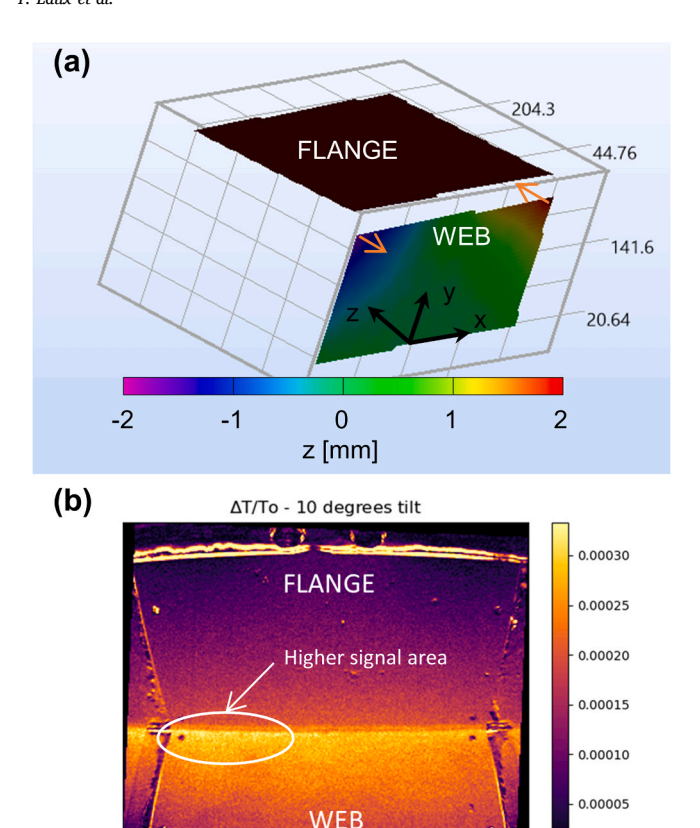


Fig. 13. Indication for twisted web; (a) reconstructed DIC z coordinates, and (b) TSA stress metric for $\theta=10^\circ$.

component error map histograms were produced for both the initial (idealised) and updated (distorted) FE models. The error map histograms for both models were then overlaid for all investigated load cases and for both the flange and web ROIs, as shown in Figs. 15 and 16, respectively. The modification to the FE model has, as expected, not significantly altered the strain state in the flange, as shown in Fig. 15. However, significant improvements have been achieved in the web ROI, as shown in Fig. 16. While the error map histograms of the initial FE model feature second non-zero peaks, associated with the ε_{yy} mismatch, as already observed in Fig. 12 (a), errors in the updated models are all centred around a single peak with $\mu_e \approx 0$. Hence, the model update has

improved the match for all investigated load cases between 20 % and 85 %, based on $\mu_e.$ The improved match of the updated web geometry (see Fig. 14), combined with improved strain error map histograms (see Fig. 16), demonstrate that the updated FE model is overall a better representation of the physical T-joint. It confirms that the hypothesis that the shape mismatch between the physical and idealised T-joint in the FE model was a key reason for the observed discrepancies in the strain state in the web ROI. Moreover, it provides a demonstration of the effectiveness of the full-field data fusion approach.

6.2. TSA based evaluation

Both the adiabatic and non-adiabatic (includes heat transfer) numerical thermoelastic response obtained from the initial and updated FE models (see Section 4.2), were compared against the experimental thermoelastic response (see Section 3.2). Fig. 17 shows a comparative assessment of data along a line of the T-joint cross section in the centre of the web and flange ROIs. It is observed that the updated FE model improves the match between the predicted and experimental thermal response for all three tilt angles. This further supports the hypothesis that the discrepancies between the initial model and experimental data, as discussed in Section 5, were due to the shape discrepancy between the model and the actual T-joint. In addition, the difference in the predicted thermoelastic response between the adiabatic and non-adiabatic FE models suggest that heat transfer cannot be neglected for quantitative model validation. Adiabatic conditions are not achieved in the experiment due to the relatively low loading frequency of 1 Hz in combination with stress gradients in the structure that drive the heat transfer, particularly the through-thickness gradient, which is induced by plate bending. The FE model that includes heat transfer is generally in closer agreement with the experimental data. A perfect match cannot be expected, as the model relies on thermal material properties of steel taken from literature (see Table 2) and does not include the effect of the paint coating [55] or any motion blur resulting from the cyclic loading [56]. The apparent large difference between model predictions and experimental results for the web in the upright case shown in Fig. 17 (a) is because the thermoelastic response is close to zero, and as $\Delta T/T_0$ is an absolute modulus value it cannot be less than zero. Therefore, in the presence of noise, an offset (bias) occurs as shown in Fig. 17 (a).

6.3. Yield assessment and final collapse

Having demonstrated that the DIC and TSA experimental and model data are in good agreement up to $P_1=25~\rm kN$ / $P_3=20.825~\rm kN$, the

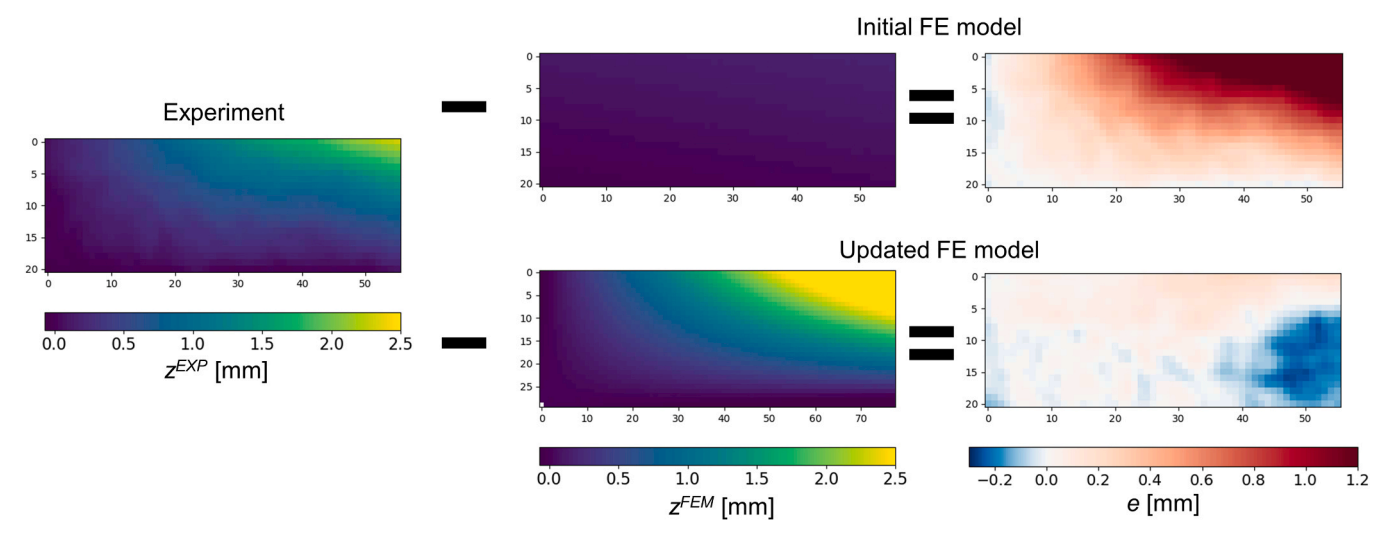


Fig. 14. Comparison of reconstructed z-coordinates in the web for the physical T-joint and the initial and distorted (updated) T-joint FE models.

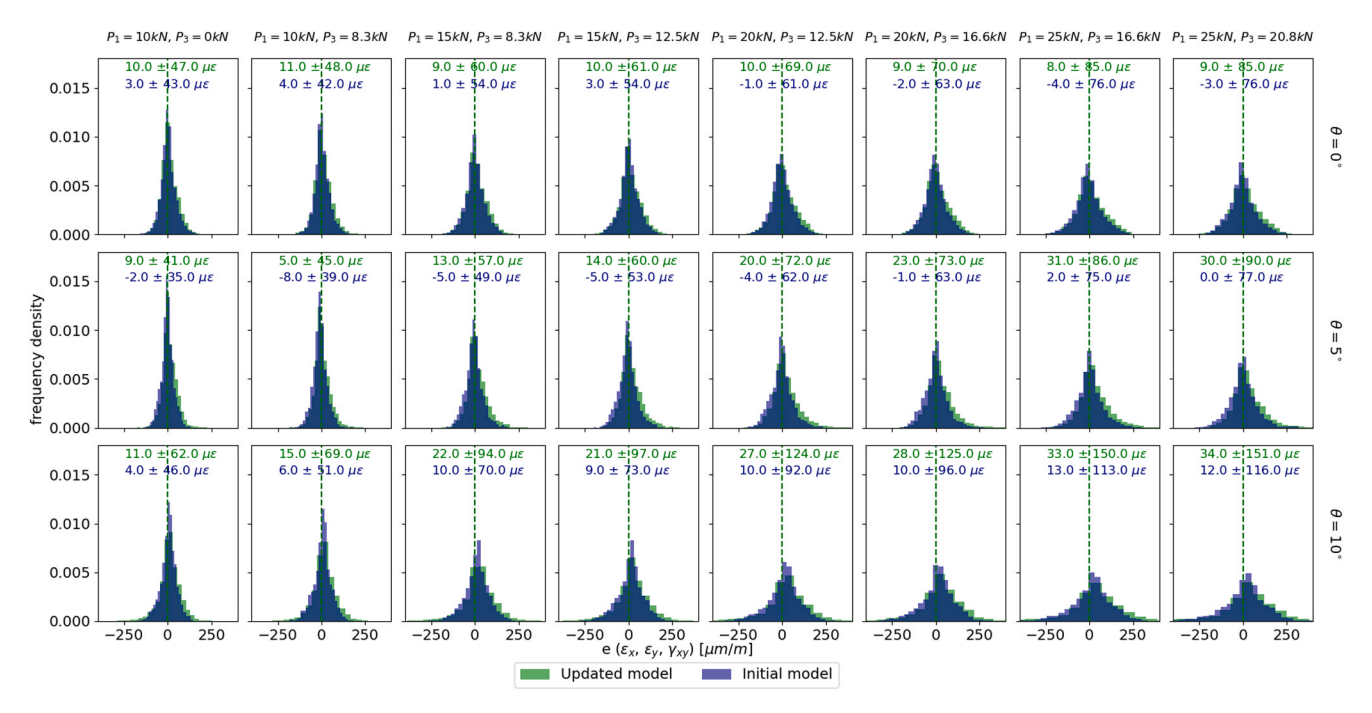


Fig. 15. Combined ε_{xx} , ε_{yy} and γ_{xy} strain error map histograms of the flange ROI for the initial and updated (distorted) T-joint FE model.

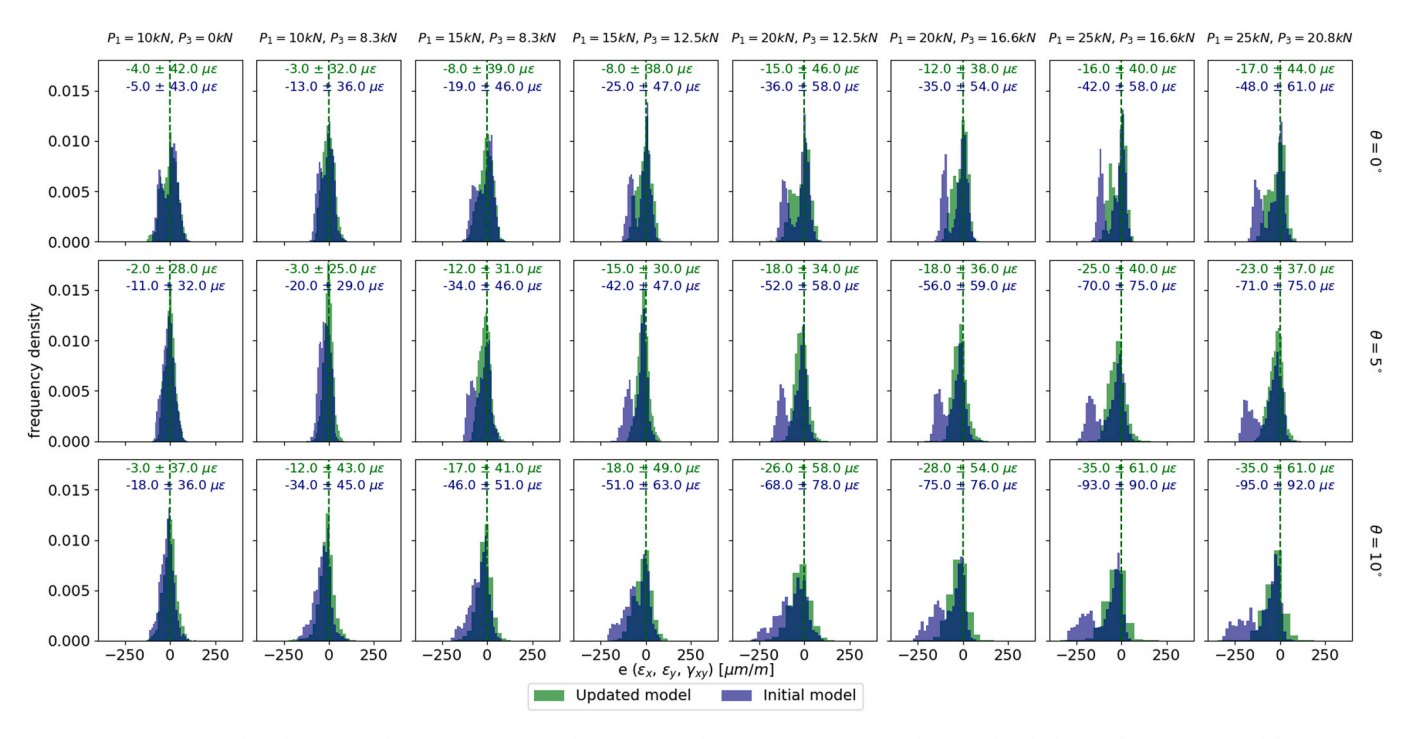


Fig. 16. Combined ε_{xx} , ε_{yy} and γ_{xy} strain error map histograms of the web ROI for the initial and updated (distorted) T-joint FE model.

 $\theta=10^\circ$ tilt angle cases up to structural collapse at $P_1=37.5~\rm kN$ / $P_3=31.24~\rm kN$ were investigated. A photograph of the unloaded specimen post-yielding is shown in Fig. 18, where loss of load carrying capability was associated with large-scale plastic deformation in the web close to the welded joint.

It is now possible to investigate if the onset of yielding prior to final collapse can be determined from the DIC and/or TSA full-field measurements. For the DIC based assessment, the equivalent von Mises strains, $\varepsilon_{\rm V}$, in the web were obtained as shown in Fig. 19 (a). In the experimental DIC data, $\varepsilon_{\rm V}$ exceeds the equivalent yield strain, $\varepsilon_{\rm V}=1690$ $\mu\varepsilon_{\rm V}$, at $P_1=30$ kN, which closely aligns with the initial yield prediction

from the elastic FE model. To further visualise the onset of nonlinear material behaviour, the mean of the $\varepsilon_{\rm v}$ field was evaluated as a function of the applied load case. Fig. 19 (b) shows that the rate of change in the mean of $\varepsilon_{\rm v}$ increases rapidly after $\varepsilon_{\rm v}>\varepsilon_{\rm y}$ at $P_1=30$ kN, which confirms the onset of nonlinear material behaviour, i.e. yielding. DIC $\varepsilon_{\rm v}$ strain measurements can therefore be used to identify initial localised areas of yielding.

Similarly, the experimental mean $\frac{\Delta T}{T_o}$ from TSA for each loading step was computed and the percentage difference relative to the first load step at $P_1=10$ kN was plotted in Fig. 19 (b). As the cyclic loading regime was kept constant throughout the testing, according to Eqs. (1)

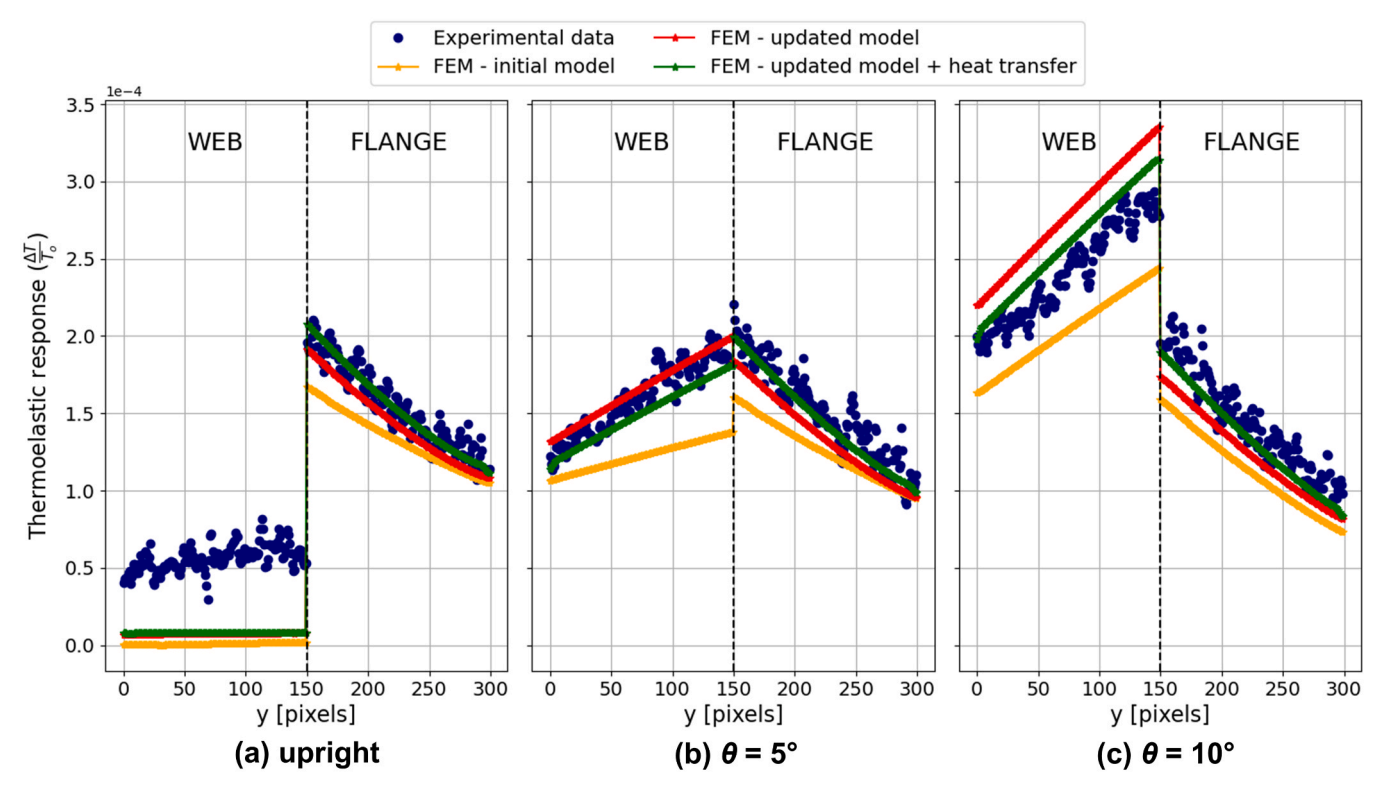


Fig. 17. TSA experimental and numerical results for $P_1 = -6 \pm 5$ kN and f = 1 Hz at different tilt angles; (a) upright, (b) $\theta = 5^{\circ}$, and (c) $\theta = 10^{\circ}$.

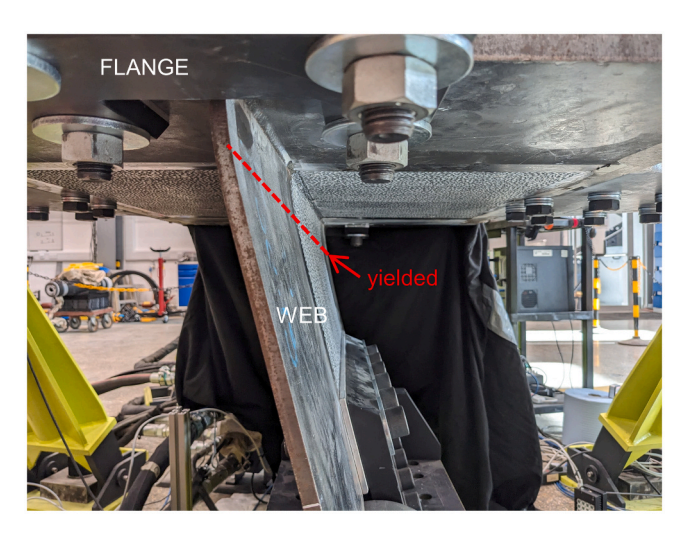


Fig. 18. T-joint after final collapse associated with permanent, plastic deformation in the web close to the joint.

and (2), changes in ΔT are either caused by stress redistribution resulting from damage and/or geometry changes caused by permanent deformation and/or by changes in K resulting from plastic straining [47], [48], all providing an indication of the onset of plastic deformation, i.e. yielding. It is observed from Fig. 19 (b), that a rapid increase in the thermoelastic response coincides with an increase in $\varepsilon_{\rm v}$, ultimately leading to a 12 % change at the final load step of $P_1=37.5~{\rm kN}$, corroborating the findings from the DIC. The thermoelastic response prior to $P_1=30~{\rm kN}$ increases by about 2 – 4 %, which may be attributed to localised yielding but most likely is within the measurement uncertainty, especially given that the specimen has been displaced in between TSA measurements by a compliant loading system that may not be fully reversible at low loads due to various pinned and bolted connections and its considerable inertia. Nevertheless, the change in the thermoelastic

response at the known yield point is significant. Thus, it is established that TSA can also be used as a monitoring technique to identify the onset of yielding, or more generally, the initiation of material nonlinearities and permanent deformation.

7. Conclusions and future work

The potential of integrated testing and modelling at the substructure scale, utilising full-field imaging and data fusion, has been demonstrated on a steel T-joint specimen with geometry and stiffness representative of a composite wind turbine blade spar cap/web T-joint substructure. To conduct the multiaxial substructure testing, the Structures 2025 facility was developed and commissioned. The facility comprises reconfigurable reaction frames installed on a strong floor, hydraulic actuators and multi-station controller, along with various white light and infrared cameras for Digital Image correlation (DIC) and Thermoelastic Stress Analysis (TSA), respectively.

Innovative image-based approaches to structural evaluation enabled a comprehensive and quantitative assessment of a substructural FE model. The new approaches reliably and efficiently highlighted discrepancies between the experimental and modelling data due to a manufacturing/welding induced mismatch in geometry between the experimental and the idealised T-joint in the FE model. Furthermore, the full-field data fusion provided the means to comprehensively quantify improvements made to the FE model by accounting for the actual, distorted geometry of the steel T-joint. The research represents an important step towards integrating virtual testing and full-field imaging facilitated by data fusion at the higher length scales of the testing pyramid for the design, development, and certification programmes of next-generation, high-performance structures across, for example, the wind energy, aerospace, automotive, marine, or construction sectors.

The research described above provides guidelines to obtain robust DIC measurements in large structures testing to reduce aleatoric and systematic errors with a focus on mitigating deleterious effects from heat waves by employing fans, thermal shields, and image averaging

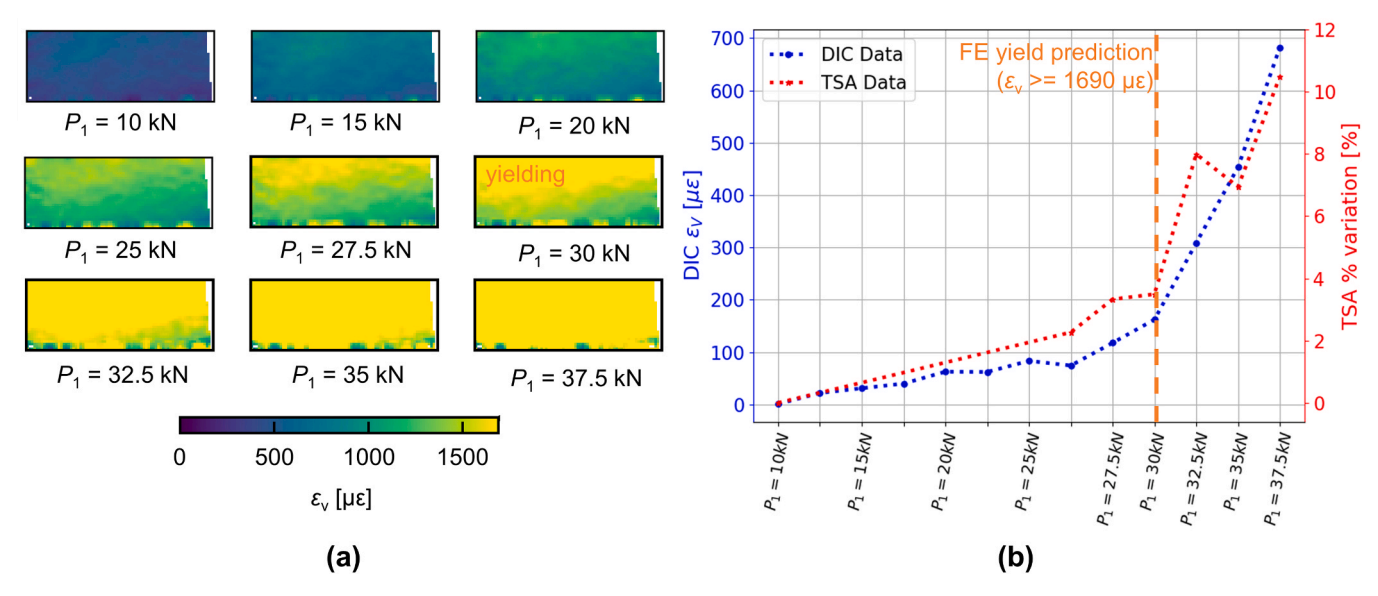


Fig. 19. Failure assessment of the web at $\theta = 10^{\circ}$; (a) ε_{v} strain fields associated with increasing loading, and (b) evolution of the mean equivalent von Mises strains (ε_{v}) and % change of the thermoelastic response (ΔT) with increasing load levels.

procedures. A like-for-like, quantitative comparison between experimental and modelling data is then enabled by the application of a recently developed framework in which synthetic deformed images are generated using an FE-based stereo DIC simulator. The approach enables identification and elimination/reduction of inconsistencies between the experimental and numerical data sets that can result in spurious differences that are difficult to interpret.

To overcome the requirement of prevailing adiabatic conditions in the thermomechanical coupling required for TSA, a modelling framework was adopted that included heat transfer. It was demonstrated that the thermomechanical model obviated the need for using relatively high loading frequencies to achieve adiabatic conditions, which may be undesirable, unachievable (or both) in large structural tests. Hence, a direct like-for-like comparison of the experimentally measured and numerically predicted thermoelastic response was achieved.

Lastly, the importance of accounting for experimental boundary conditions, including actuator kinematics and weight, and for real specimen geometries is essential in reducing model discrepancies to a level where more intricate/detailed structural evaluations and model assessments can be conducted.

In future work, the new Structures 2025 facility, along with the imaging, data fusion, and modelling approaches will be extended and applied to a composite wind turbine blade spar cap/web T-joint specimen. The aim will be to characterise the complex mechanical response and failure behaviour of the composite T-joint, and to provide information-rich data for the development and validation of advanced composite modelling frameworks for virtual testing at the substructural level of the testing pyramid.

CRediT authorship contribution statement

Duncan A. Crump: Writing - review & editing, Supervision,

Conceptualization. Andrew F. Robinson: Writing – review & editing, Funding acquisition, Conceptualization. Ole T. Thomsen: Writing review & editing, Supervision, Project administration, Funding acquisition, Conceptualization. Tobias Laux: Writing - original draft, Visualization, Validation, Supervision, Software, Project administration, Methodology, Investigation, Formal analysis, Data curation, Conceptualization. Janice M. Dulieu-Barton: Writing - review & editing, Supervision, **Project** administration, Funding acquisition, Conceptualization. Geir Ólafsson: Investigation. Stephen W. Boyd: Writing - review & editing, Funding acquisition, Conceptualization. Riccardo Cappello: Writing - review & editing, Visualization, Validation, Software, Methodology, Investigation, Formal analysis, Data curation, Conceptualization. Jack S. Callaghan: Visualization, Software, Methodology, Conceptualization.

Declaration of Competing Interest

The authors declare that they have no known competing financial interests or personal relationships that could have appeared to influence the work reported in this paper.

Acknowledgements

This research was supported by the EPSRC strategic equipment grant 'Structures 2025 – A High Fidelity, Data Rich, Paradigm for Structural Testing' (S2025, EP/R008787/1) and the EPSRC Programme Grant 'Certification for Design – Reshaping the Testing Pyramid' (CerTest, EP/S017038/1). The authors also thank Dr Alexander Marek, University of Southampton, and Dr Pascal Lava, MatchID, for their help with the DIC system set-up and the many insightful discussions. The help of Andy Morgan, LSTL technician, in setting up the experiment, and Dr Tim Harrell, in the design of the test frames, is also gratefully acknowledged.

Appendix

Table A.1DIC post processing settings.

DIC software	MatchID 2024.2.3[42]	
Correlation criterion	Zero-normalised sum of squared Differences (ZNSSD)	
Sub-pixel interpolation	Local Bicubic Spline Interpolation	
Subset shape function	Affine	
Stereo transformation method	Affine	
Subset size	71	
Step size	35	
Strain window size	5	
Strain tensor	Logarithmic Euler – Almansi	
Strain interpolation	Bilinear Quadrilateral (Q4)	

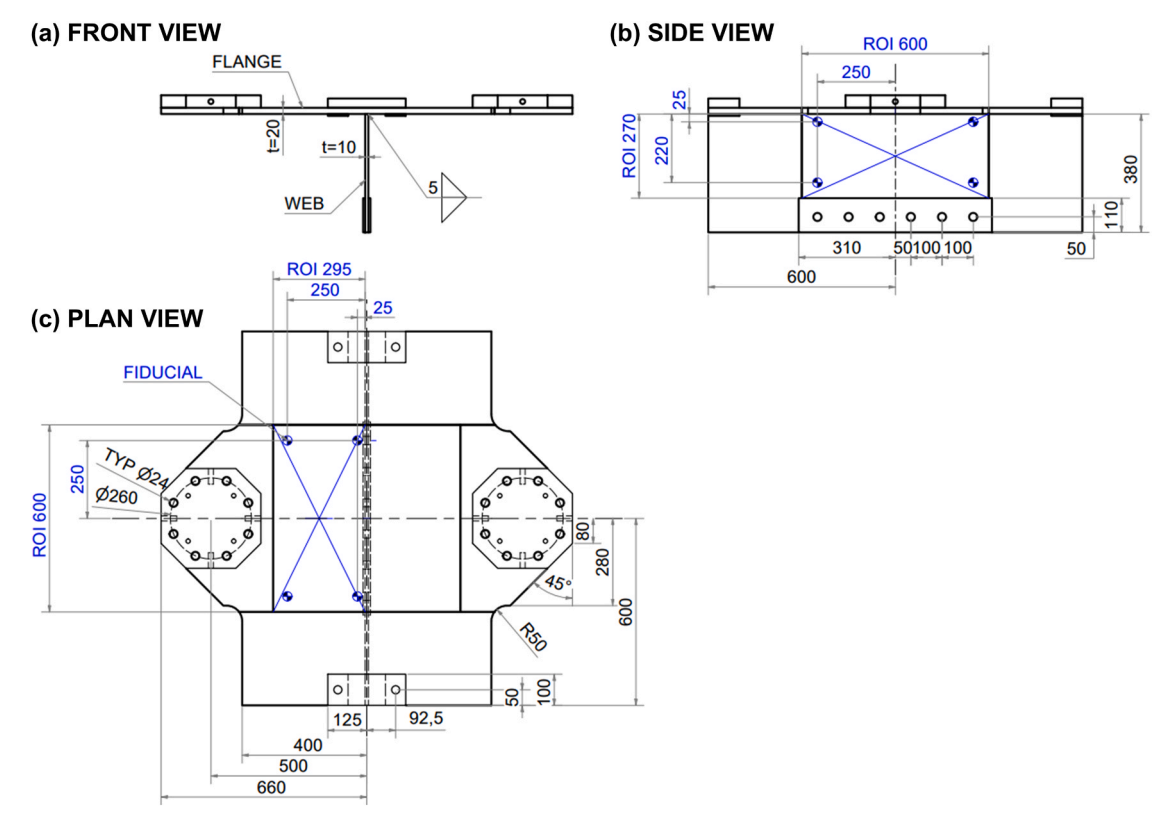


Figure A.1. Technical drawing of steel T-joint mock-up specimen including location of ROIs (blue) and fiducial markers (dimensions in mm).

Data availability

The data is available from the University of Bristol data repository (https://doi.org/10.5523/bris.t5so4c5yw9p527b7dnkkwn80n).

References

- Department of Defense United States of America. MIL-HDBK-17-3F Compos Mater Handb Vol 3 2002.
- [2] Rouchon J. Certification of large aircraft composite structures, recent progress and new trends in compliance philosophy. 17th ICAS Congr, Stockh 1990:1439–47. (htt p://www.icas.org/ICAS_ARCHIVE/ICAS1990/ICAS-90-1.8.1.pdf).
- [3] DNV-GL, "DNV-ST-0376 Rotor blades for wind turbines," 2021.
- [4] Ostergaard MG, Ibbotson AR, Roux OLe, Prior AM. Virtual testing of aircraft structures. CEAS Aeronaut J Sep. 2011;1(1–4):83–103. https://doi.org/10.1007/ s13272-011-0004-x.
- [5] Lopes CS, González C, Falcó O, Naya F, LLorca J, Tijs B. Multiscale virtual testing: the roadmap to efficient design of composites for damage resistance and tolerance. CEAS Aeronaut J 2016;7(4):607–19. https://doi.org/10.1007/s13272-016-0210-7.
- [6] Furtado C, Catalanotti G, Arteiro A, Gray PJ, Wardle BL, Camanho PP. Simulation of failure in laminated polymer composites: Building-block validation. Compos Struct 2019;226.

- [7] Falcó O, Ávila RL, Tijs B, Lopes CS. Modelling and simulation methodology for unidirectional composite laminates in a Virtual Test Lab framework. Compos Struct 2018;190:137–59. https://doi.org/10.1016/j.compstruct.2018.02.016.
- [8] Laux T, et al. Modelling damage in multidirectional laminates subjected to multiaxial loading: Ply thickness effects and model assessment. Compos Struct 2021;266 (ember 2020):113766. https://doi.org/10.1016/j.compstruct.2021.113766.
- [9] El Said B. Predicting the non-linear response of composite materials using deep recurrent convolutional neural networks. Int J Solids Struct Aug. 2023;276. https://doi.org/10.1016/j.jisolstr.2023.112334.
- [10] El Said B, Hallett SR. Multiscale surrogate modelling of the elastic response of thick composite structures with embedded defects and features. Compos Struct Sep. 2018;200:781–98. https://doi.org/10.1016/j.compstruct.2018.05.078.
- [11] Bénézech J, et al. Scalable multiscale-spectral GFEM with an application to composite aero-structures. J Comput Phys Jul. 2024;508. https://doi.org/10.1016/ i.icp.2024.113013.
- [12] Waldbjoern JP, Andersen S, Hoegh JH, Berggreen C. Single-component multi-rate real time hybrid simulation pilot test on a composite structure. Eng Struct Feb. 2024;301. https://doi.org/10.1016/j.engstruct.2023.117353.
- [13] Chen Y, Zhang J, Wang F, Gao C. Hybrid substructure interacting method fusing targeted sensing data and finite element models. Eng Struct Sep. 2024;314. https:// doi.org/10.1016/j.engstruct.2024.118314.
- [14] Han Q, Zhao Y, Lu Y, Wang S. Substructure hybrid test examining the seismic response of point-supported glass façades attached to large-span spatial steel

- structures. Eng Struct Sep. 2022;266. https://doi.org/10.1016/j.
- [15] Sutton MA, Orteu JJ, Schreier H. Image correlation for shape, motion and deformation measurements. Springer,; 2009.
- [16] Dulieu-Barton JM. Thermoelastic Stress Analysis. In: Rastogi P, Hack E, editors. in Optical methods for solid mechanics. Weinheim: Wiley-VCH; 2012. ch. 8.
- [17] Laux T, Gan KW, Dulieu-Barton JM, Thomsen OT. Ply thickness and fibre orientation effects in multidirectional composite laminates subjected to combined tension/compression and shear. Compos Part A Appl Sci Manuf Jun. 2020;133. https://doi.org/10.1016/j.compositesa.2020.105864.
- [18] Camanho PP, Maimí P, Dávila CG. Prediction of size effects in notched laminates using continuum damage mechanics. Compos Sci Technol 2007;67(13):2715–27. https://doi.org/10.1016/j.compscitech.2007.02.005.
- [19] Taireja R. Manufacturing defects in composites and their effects on performance. in Polymer Composites in the Aerospace Industry. Elsevier.; 2019. p. 83–97. https://doi. org/10.1016/B978-0-08-102679-3.00004-6.
- [20] R. Janeliukstis and X. Chen, "Review of digital image correlation application to large-scale composite structure testing," Sep. 01, 2021, Elsevier Ltd. doi: 10.10 16/j.compstruct.2021.114143.
- [21] Callaghan JS, Crump D, Nielsen AS, Thomsen OT, Dulieu-Barton JM. Quantitative Full-Field Data Fusion for Evaluation of Complex Structures. Exp Mech 2023; (0123456789). https://doi.org/10.1007/s11340-023-00973-8.
- [22] Gardner NW, Hilburger MW, Haynie WT, Lindell MC, Waters WA. Digital image correlation data processing and analysis techniques to enhance test data assessment and improve structural simulations. SCITECH 2018.
- [23] Chen X, Berring P, Madsen SH, Branner K, Semenov S. Understanding progressive failure mechanisms of a wind turbine blade trailing edge section through subcomponent tests and nonlinear FE analysis. Compos Struct Apr. 2019;214: 422–38. https://doi.org/10.1016/j.compstruct.2019.02.024.
- [24] S. Laustsen, E. Lund, and L. Ku, "Failure behaviour of grid-scored foam cored composite sandwich panels for wind turbine blades subjected to realistic multiaxial loading conditions," 2014, doi: 10.1177/1099636214541367.
- [25] Laustsen S, Lund E, Kühlmeier L, Thomsen OT. Development of a high-fidelity experimental substructure test rig for grid-scored sandwich panels in wind turbine blades. Strain 2014;50(2):111–31. https://doi.org/10.1111/str.12072.
- [26] Serra J, Pierré JE, Passieux JC, Périé JN, Bouvet C, Castanié B. Validation and modeling of aeronautical composite structures subjected to combined loadings: The VERTEX project. Part 1: Experimental setup, FE-DIC instrumentation and procedures. Compos Struct 2017;179:224–44. https://doi.org/10.1016/j. compstruct.2017.07.080.
- [27] Serra J, et al. Validation and modeling of aeronautical composite structures subjected to combined loadings: The VERTEX project. Part 2: Load envelopes for the assessment of panels with large notches. Compos Struct 2017;180:550–67. https://doi.org/10.1016/j.compstruct.2017.08.055.
- [28] Zhang WX, LI ST, Wang X, Zhang YY, Yi WJ. Beam torsion effect of monolithic precast concrete beam-column substructures during progressive collapse. Eng Struct Mar. 2023;278. https://doi.org/10.1016/j.engstruct.2022.115457.
- [29] Paynter RJH, Dutton AG. The use of a second harmonic correlation to detect damage in composite structures using thermoelastic stress measurements. Strain May 2003;39(2):73–8. https://doi.org/10.1046/j.1475-1305.2003.00056.x.
- [30] Crump DA, Dulieu-Barton JM. Assessment of Non-adiabatic Behaviour in Thermoelastic Stress Analysis of Composite Sandwich Panels. Exp Mech Sep. 2012; 52(7):829–42. https://doi.org/10.1007/s11340-012-9601-9.
- [31] Fruehmann RK, Dulieu-Barton JM, Quinn S, Peton-Walter J, Mousty PAN. The application of thermoelastic stress analysis to full-scale aerospace structures. in *Journal of Physics: Conference Series*. Institute of Physics Publishing,; 2012. https://doi.org/10.1088/1742-6596/382/1/012058.
- [32] Rajic N, Galea S. Thermoelastic stress analysis and structural health monitoring: An emerging nexus. Struct Health Monit Jan. 2015;14(1):57–72. https://doi.org/ 10.1177/1475921714548936.
- [33] Lava P, Jones EMC, Wittevrongel L, Pierron F. Validation of finite-element models using full-field experimental data: Levelling finite-element analysis data through a

- digital image correlation engine. Strain 2020;56(4):1–17. https://doi.org/
- [34] Myers T, Sutton MA, Schreier H, Tofts A, Kattil SR. "Direct Pointwise Comparison of FE Predictions to Stereo DIC Measurements: Developments and Validation Using Double Edge-Notched Tensile Specimen,". CMES - Comput Model Eng Sci 2024;140 (2):1263–98. https://doi.org/10.32604/cmes.2024.048743.
- [35] Brazier LG. On the flexure of thin cylindrical shells and other 'thin' sections. Proc R Soc Lond Ser A, Contain Pap A Math Phys Character 1927;116(773):104–14. https://doi.org/10.1098/rspa.1927.0125.
- [36] Cox K, Echtermeyer A. Structural Design and Analysis of a 10MW Wind Turbine Blade. Energy Procedia 2012;24:194–201. https://doi.org/10.1016/j. egypro.2012.06.101
- [37] J.S. Callaghan, "High fidelity testing of wind turbine blade substructures," PhD Thesis, University of Southampton, 2022. Accessed: Oct. 11, 2024. [Online]. Available: https://enrints.soton.ac.uk/467769/)
- [38] Shenoi RA, Read PJCL, Hawkins GL. Fatigue failure mechanisms in fibre-reinforced plastic laminated tee joints. Int J Fatigue 1995;17(6):415–26. https://doi.org/ 10.1016/0142-1123(95)98238-X.
- [39] Wang Y, Soutis C. A Finite Element and Experimental Analysis of Composite T-Joints Used in Wind Turbine Blades. Appl Compos Mater 2018;25(4):953–64. https://doi.org/10.1007/s10443-018-9711-3.
- [40] S.T. Pinho, C.G. Dávila, P.P. Camanho, L. Iannucci, and P. Robinson, "Failure models and criteria for FRP under in-plane or three-dimensional stress states including shear non-linearity," 2005. doi: NASA/TM-2005–213530.
- [41] Tsai SW, Wu EM. A general theory of strength for anisotropic materials. J Compos Mater 1971;5(1):58–80. https://doi.org/10.1177/002199837100500106.
- [42] "MatchID." [Online]. Available: (https://www.matchid.eu/).
- [43] Reu P. The art and application of DIC. Exp Tech 2012;37(February). https://doi. org/10.1111/j.1747-1567.2011.00798.x.
- [44] Robert McNeel & Associates, "Rhinoceros 3D," 2020. [Online]. Available: (https://www.rhino3d.com/).
- [45] E.M.C. Jones and M.A. Iadicola, A good practices guide for digital image correlation. 2018. doi: 10.32720/idics/gpg.ed1.
- [46] Jones EMC, Reu PL. Distortion of Digital Image Correlation (DIC) Displacements and Strains from Heat Waves. Exp Mech 2018;58(7):1133–56. https://doi.org/ 10.1007/s11340-017-0354-3.
- [47] Cappello R, Meneghetti G, Ricotta M, Pitarresi G. On the correlation of temperature harmonic content with energy dissipation in C45 steel samples under fatigue loading. Mech Mater May 2022;168. https://doi.org/10.1016/j. mechmat.2022.104271.
- [48] Quinn S, Dulieu-Barton JM, Langlands JM. Progress in thermoelastic residual stress measurement. Strain Aug. 2004;40(3):127–33. https://doi.org/10.1111/j.1475-1305.2004.00140.x.
- [49] O. Warta WSC, 'Breitenstein M. Lock-in thermography: basics and use for evaluating electronic devices and materials. 3rd ed..., 10. Springer,; 2019.
- [50] Shannon CE. "Communication in the presence of noise. *Proc IRE* 1949;37.1:10–21.
- [51] "Abagus 2018." Dassault Systems Simulia Corp.
- [52] Cappello R, Pitarresi G, Catalanotti G. Thermoelastic Stress Analysis for composite laminates: A numerical investigation. Compos Sci Technol Aug. 2023;241. https://doi.org/10.1016/j.compscitech.2023.110103.
- [53] Howse J. OpenCV computer vision with python, 27. Packt Publishing Birmingham.: 2013.
- [54] Jones E., Oliphant T., and Peterson P., "SciPy: Open source scientific tools for python," 2001. [Online]. Available: (https://docs.scipy.org/doc/scipy/reference/generated/scipy.optimize.least squares.html).
- [55] Robinson AF, Dulieu-Barton JM, Quinn S, Burguete RL. Paint coating characterization for thermoelastic stress analysis of metallic materials. Meas Sci Technol 2010;21(8). https://doi.org/10.1088/0957-0233/21/8/085502.
- [56] Wang W, Fruehmann RK, Dulieu-Barton JM. Application of Digital Image Correlation to Address Complex Motions in Thermoelastic Stress Analysis. Strain Oct. 2015;51(5):405–18. https://doi.org/10.1111/str.12151.
- [57] Laux T, et al. Testing of a wind turbine blade spar cap to web joint subcomponent subjected to multiaxial loading. 23rd Int Conf Compos Mater (ICCM23) 2023.